



Infrared Selection of Obscured Active Galactic Nuclei in the COSMOS Field

Yu-Yen Chang^{1,2}, Emeric Le Floc'h¹, Stéphanie Juneau¹, Elisabete da Cunha³, Mara Salvato⁴, Francesca Civano⁵, Stefano Marchesi⁶, Olivier Ilbert⁷, Yoshiki Toba², Chen-Fatt Lim^{2,8}, Ji-Jia Tang^{2,8}, Wei-Hao Wang², Nicholas Ferraro^{2,9},

Megan C. Urry¹⁰, Richard E. Griffiths¹¹, and Jeyhan S. Kartaltepe¹²

¹ CEA Saclay, DSM/Irfu/Service d'Astrophysique, Orme des Merisiers, F-91191 Gif-sur-Yvette Cedex, France; yuyenchang.astro@gmail.com

² Academia Sinica Institute of Astronomy and Astrophysics, P.O. Box 23-141, Taipei 10617, Taiwan

³ The Australian National University, Mt Stromlo Observatory, Cotter Rd, Weston Creek, ACT 2611, Australia

⁴ Max Planck Institut für Plasma Physik und Excellence Cluster, D-85748 Garching, Germany

⁵ Harvard-Smithsonian Center for Astrophysics, 60 Garden Street, Cambridge, MA 02138, USA

⁶ Department of Physics & Astronomy, Clemson University, Clemson, SC 29634, USA

⁷ Aix-Marseille Université, CNRS, LAM (Laboratoire d'Astrophysique de Marseille) UMR 7326, F-13388, Marseille, France

⁸ Graduate Institute of Astrophysics, National Taiwan University, No.1 Section 4 Roosevelt Rd., Taipei 10617, Taiwan

⁹ Department of Astronomy, University of Virginia, 530 McCormick Rd., Charlottesville, VA 22904, USA

¹⁰ Yale Center for Astronomy and Astrophysics, 260 Whitney Avenue, New Haven, CT 06520, USA

¹¹ Department of Physics & Astronomy, University of Hawaii at Hilo, 200 W. Kawili Street, Hilo, HI 96720, USA

¹² School of Physics and Astronomy, Rochester Institute of Technology, 84 Lomb Memorial Drive, Rochester, NY 14623, USA

Received 2017 July 5; revised 2017 October 16; accepted 2017 October 31; published 2017 December 7

Abstract

We present a study of the connection among black hole accretion, star formation, and galaxy morphology at $z \leq 2.5$. We focus on active galactic nuclei (AGNs) selected by their mid-IR power-law emission. By fitting optical to far-IR photometry with state-of-the-art spectral energy distribution (SED) techniques, we derive stellar masses, star formation rates, dust properties, and AGN contributions in galaxies over the whole COSMOS field. We find that obscured AGNs lie within or slightly above the star-forming sequence. We confirm our previous finding about compact host galaxies of obscured AGNs at $z \sim 1$, and find that galaxies with 20%–50% AGN contributions tend to have smaller sizes, by $\sim 25\%$ – 50% , compared to galaxies without AGNs. Furthermore, we find that a high merger fraction of up to 0.5 is appropriate for the most luminous ($\log(L_{\text{IR}}/L_{\odot}) \sim 12.5$) AGN hosts and non-AGN galaxies, but not for the whole obscured AGN sample. Moreover, the merger fraction depends on the total and star-forming IR luminosity, rather than on the decomposed AGN infrared luminosity. Our results suggest that major mergers are not the main driver of AGN activity, and therefore obscured AGNs might be triggered by internal mechanisms, such as secular processes, disk instabilities, and compaction in a particular evolutionary stage. We make the SED modeling results publicly available.

Key words: galaxies: active – galaxies: star formation – infrared: galaxies

1. Introduction

One of the most important issues in studies of galaxy evolution is the connection between the formation of stars in galaxies and the fueling of nuclear activity. Star formation arises from the collapse of cold molecular clouds while active galactic nucleus (AGN) activity is caused by the accretion of matter onto supermassive black holes. Though star formation and AGN activity occur on very different scales, AGNs could be involved in the process of quenching star formation. Previous results revealed that X-ray and optically selected AGNs reside in galaxies harboring sustained star formation activity (Harrison et al. 2012; Mullaney et al. 2012; Santini et al. 2012; Juneau et al. 2013; Rosario et al. 2013; Stanley et al. 2015; Mahoro et al. 2017). Furthermore, although high-luminosity AGNs seem to be connected to violent events and may reside in galaxies more often involved in major mergers (Kartaltepe et al. 2012; Treister et al. 2012; Fan et al. 2016), the majority of X-ray-selected AGNs appear to live mostly in disk-dominated isolated systems (e.g., Cisternas et al. 2011; Kocevski et al. 2012), implying that the bulk of supermassive black hole accretion is likely driven by internal processes and not by major mergers.

Although the results reported above have been mostly drawn from populations of unobscured AGNs according to X-ray observations, it has recently been suggested that obscured AGNs,

which are not well-sampled by X-ray surveys, may reside in different environments. For instance, Compton-thick AGNs hidden by extreme column densities ($N_H > 10^{24} \text{ cm}^{-2}$) tend to show a fraction of disturbed morphologies increasing with obscuration (Kocevski et al. 2015; Lanzuisi et al. 2015a; Ricci et al. 2015, 2017). This suggests that Compton-thick AGNs can be in a phase of obscured supermassive black hole growth following a merger event. Current samples of obscured AGNs are mostly limited to moderate obscuration by X-ray detections, which are selected from gas column density measurements (Lusso et al. 2011, 2013; Bongiorno et al. 2014; Merloni et al. 2014; Brusa et al. 2015). Compton-thick AGNs are found by deep X-ray observations (Brightman et al. 2014), but the limited field sizes also limit detections.

Another approach to exploring obscured AGNs is from infrared (IR) observations, which can provide complementary samples compared to X-ray data (Coppin et al. 2010; Mateos et al. 2012; Del Moro et al. 2016). IR-selected AGNs can be identified from their mid-IR (MIR) power-law emission using *Spitzer*/IRAC photometry (Lacy et al. 2004; Stern et al. 2005; Lacy et al. 2007, hereafter L07; Donley et al. 2012, hereafter D12). This technique can be applied up to $z \sim 2.5$ or even higher redshifts (Messias et al. 2012). Since this approach only relies on the detection of dust continuum emission in the IR, it can unveil AGNs suffering very strong obscuration in the X-rays, including AGNs even missed by the deepest X-ray

observations obtained to date. A proxy for obscuration can be inferred using the IR to X-ray luminosity ratio (or lower limit if there is no X-ray detection), where the AGN IR luminosity can be estimated using state-of-the-art spectral energy distribution (SED) fitting techniques as discussed in Mullaney et al. (2011), Kirkpatrick et al. (2012, 2013), Dale et al. (2014), Hernán-Caballero et al. (2015), Kirkpatrick et al. (2015), Calistro Rivera et al. (2016), and Huang et al. (2017). Obscured AGNs can then be selected as sources that are underluminous in the X-rays relative to their bolometric luminosity inferred from the IR (Messias et al. 2014).

The morphologies of host galaxies have been characterized using two-dimensional surface brightness modeling and non-parametric morphology methods, and visual classification. Virani et al. (2000) found that there are no significant differences between their control and active Seyfert host galaxies in terms of light asymmetries. Grogin et al. (2005) showed that ~ 150 X-ray AGNs have bulge-dominated morphologies from their concentration and asymmetry up to $z \sim 1.3$. Pierce et al. (2007) found that 94 X-ray-selected AGNs with $0.2 < z < 1.2$ mostly reside in E/S0/Sa galaxies, while IR-selected AGNs showed no clear preference for host morphology from nonparametric measures. Georgakakis et al. (2008) studied Compton-thick AGNs with $0.4 < z < 0.9$ and suggested that a large fraction of post-starbursts and red cloud galaxies have evidence for at least moderate levels of AGN obscuration. In order to avoid AGN contamination, Gabor et al. (2009) decomposed ~ 400 X-ray-selected AGNs into AGN point sources and galaxy light at $0.3 < z < 1.0$, and found that X-ray-selected AGN host morphologies span a substantial range that peaks between those of bulge-dominated and disk-dominated systems. Böhm et al. (2013) also decomposed ~ 200 type 1 X-ray AGN images at $z \sim 0.7$ into nucleus and host components, and found that active and inactive galaxies show similar distributions in the nonparametric measure space after decomposition. Villforth et al. (2014) added simulated AGNs to a stellar mass-matched control sample at $0.5 < z < 0.8$ to show that X-ray-selected AGN hosts and control sample galaxies have comparable asymmetries, Sérsic indices, and ellipticities. At higher redshift, Schawinski et al. (2011) considered point-source components for 57 X-ray AGN hosts with $1.25 < z < 2.67$, and found that half of the sample are disk dominated. Simmons et al. (2012) also chose one- or two-component models according to their fitting residuals and suggested that the majority of X-ray AGN host galaxies are disk dominated. Fan et al. (2014) analyzed 35 X-ray-selected AGNs at $z \sim 2$ based on point-source-subtracted images and suggested that all distributions of the morphological parameters of AGN hosts are consistent with their control sample. Rosario et al. (2015) showed that X-ray AGN hosts are slightly diskier and more disturbed than massive inactive galaxies at $z \sim 1$, and show a red central light enhancement at $z \sim 2$. They also demonstrated that the central excess is likely due to the bulge and the two-component model may underestimate the Sérsic index, driving the main stellar components toward disk-dominated profiles. Bruce et al. (2016) found that the structural parameters of X-ray-selected AGN hosts are indistinguishable from the general galaxy population, but have significantly higher bulge fractions beyond $z \sim 1.5$. Villforth et al. (2017) created a control sample of mock AGNs to compare with 20 optically and X-ray-selected luminous AGNs at $z \sim 0.6$, and found no enhanced disturbance in the AGNs relative to the control sample. According to these previous studies, the relation

between morphology and AGN activity is still unclear, largely because it depends on sample selection, redshift, and techniques used to measure morphology and AGN activity.

Recently, we explored the optical-light radial profile from an IR-selected sample, and found that obscured AGN hosts at $z \sim 1$ are more compact than a control sample of star-forming galaxies at the same stellar mass and redshift bins (Chang et al. 2017). Internal secular processes over long timescales could play a dominant role, but the potential impact of violent disk instabilities (VDIs) in gas-rich disks has also been discussed recently in the literature. Indeed, these VDIs are believed to result in highly clumpy galaxies such as frequently observed at $z > 1$. The possible migration of their giant star-forming clumps toward their central region could lead to the quick formation of a dense stellar component (Dekel et al. 2009; Ceverino et al. 2010), which may also be accompanied by a phase of gas compaction (Tacchella et al. 2016), producing blue nuggets (Zolotov et al. 2015), and potentially affecting the fueling of central AGNs (Dubois et al. 2015).

In this paper, we extend our previous study to a general comparison with star formation, AGN fraction, and obscuration in a complete MIR-selected sample. We compare the physical properties of AGN hosts with those of normal star-forming galaxies by using both spectral energy distribution and morphology-fitting techniques. Following the morphology studies in Chang et al. (2017), we quantify the structural parameters of obscured IR-selected AGN (IR-AGN) hosts and present their visual classification result. The structure of this paper is as follows. In Section 2, we describe the data and our selection. We present our SED-fitting results as well as the comparison between normal star-forming and AGN host galaxies in Section 3. We present a morphology analysis of AGN hosts, based on two-dimensional fitting, nonparametric method, and visual classification in Section 4. The discussion is presented in Section 5, followed by a summary in Section 6. We use AB magnitudes and the cosmological parameters $(\Omega_M, \Omega_\Lambda, h) = (0.30, 0.70, 0.70)$ and adopt the Chabrier (2003) stellar initial mass function.

2. Data and Sample Selection

2.1. MIR Galaxies and IR AGNs

Our sample is based on an MIR $24\mu\text{m}$ selection ($S_{24\mu\text{m}} \gtrsim 80\mu\text{Jy}$; Le Floc'h et al. 2009) and contains 36,670 MIR galaxies in the Cosmic Evolution Survey (COSMOS; Scoville et al. 2007) field. We match all of the MIR galaxies with the COSMOS2015 catalog (Ilbert et al. 2013; Laigle et al. 2016) to obtain photometry from the optical to the far-IR (FIR). There are 30,212 redshifts, which are first taken from the *Chandra* Legacy Survey (6.66%; Salvato et al. 2011; Civano et al. 2016; Marchesi et al. 2016), then from available spectroscopic redshifts (30.14%); otherwise, we use the COSMOS2015 photometric redshifts (63.19%; Laigle et al. 2016). We found that the fraction of outliers ($\eta = 2.9\%$) and the accuracy ($\sigma_{\text{NAMD}} = 0.002$) are reliable and good (see Ilbert et al. 2009; Salvato et al. 2011 for more details) by comparing spectroscopic and photometric redshifts.

We selected IR power-law AGN candidates as sources according to a color-color selection, which was first introduced by Lacy et al. (2004). In Figure 1, the cross symbols show objects with IRAC F_ν flux densities monotonically rising from 3.6 to $8\mu\text{m}$. We selected most ($>99\%$) of these power-law AGNs by avoiding contamination from normal galaxies and

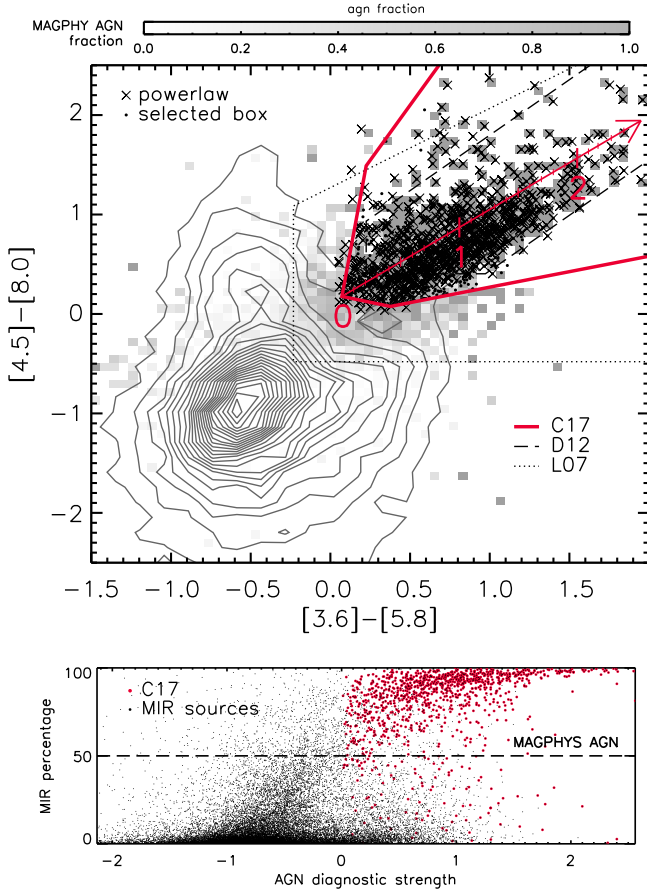


Figure 1. Upper panel: IR-AGN selection in the color-color plot at $z \leq 2.5$. The cross symbols represent galaxies with monotonically rising MIR SEDs. The black dots are our IR-selected AGNs according to the red box. The contour shows the major population. The gray coding shows the AGN fractions of the dominant MIR AGNs according to the SED fitting. Lower panel: correlation between AGN diagnostic strength (red arrow in the upper plot) and the MIR contribution of AGNs. We adopt the red box in this paper. This technique is similar to previous color-color selections (L07, D12) and consistent with power-law or MAGPHYS AGNs.

defined a box:¹³

$$y < 2.22 \times x + 1.01, \quad (1)$$

$$y < 8.67 \times x - 0.28, \quad (2)$$

$$y > -3.33 \times x + 0.17, \quad (3)$$

$$y > 0.31 \times x - 0.06, \quad (4)$$

where $x = m_{5.8\mu\text{m}} - m_{3.6\mu\text{m}}$, $y = m_{8\mu\text{m}} - m_{4.5\mu\text{m}}$, and $m_{x\mu\text{m}}$ is in AB magnitude. There are 1,085 IR-AGNs inside the box at $z \leq 2.5$ as shown in Figure 1. Of these 1,085 IR-AGNs, 670 are in the *Chandra* Legacy Survey catalog (Civano et al. 2016; Marchesi et al. 2016). For the remaining 460 IR-AGNs, spectroscopic redshifts are available for 148 of them, and photometric redshifts are adopted for 267 of them. Our selection is comparable to previous selections (Lacy et al. 2004; L07; D12) and provides an up-to-date box according to the latest IRAC measurements. Here, we define “AGN diagnostic strength” along the red arrow in the upper panel of

Table 1

Sample Size of AGN Host Galaxies of X-ray-selected AGNs ($L_X(2-10 \text{ keV}) > 10^{42} \text{ erg s}^{-1}$), MAGPHYS SED AGNs (AGN Contribution of MIR Luminosity $> 50\%$ MIR from SED Fitting), and MIR-selected AGNs (this paper, D12, and L07)

Selection	X-Ray	SED	C17	D12	L07
All	1538	2288	1085	656	3340
obscured	370	620	469	342	612

Note. The columns represent the sample size of all AGN host and obscured ($L_{\text{IR,AGN}}/L_{\text{X,AGN}} > 20$) IR-AGN host galaxies at $z \leq 2.5$.

Figure 1. The values of the AGN diagnostic strength are calculated using the projected value along the peak population of the selected box. The scales are labeled in the upper panel and shown in the lower panel of Figure 1. The gray scale shows that the AGN fractions of dominant MIR AGNs (MAGPHYS AGN; AGN contribution of MIR luminosity $> 50\%$ MIR from SED fitting as shown in the lower panel in Figure 1; see Section 2.2 for more details on the SED fitting) agree with our selection. The lower plot of Figure 1 shows a good correlation with the MIR percentage of the AGN contribution estimated with the SED fitting. We show the sample size with a less strict selection by L07, a stricter selection by D12, and the X-ray selection from the *Chandra* Legacy Survey with $L_X(2-10 \text{ keV}) > 10^{42} \text{ erg s}^{-1}$ in Table 1. There are 631 AGNs selected by both X-ray ($\sim 41\%$) and our IR ($\sim 58\%$) criterion. In order to have a simple and consistent selection, we adopt the color-color selection in this paper. An updated technique by power law or MAGPHYS AGN will be considered in future works.

2.2. SED Fitting

We fit the spectral energy distributions (SEDs) of all MIR-selected galaxies with a custom version of the MAGPHYS code (da Cunha et al. 2015). MAGPHYS computes the emission from stellar populations in galaxies from the UV to near-IR consistently with the emission from dust at MIR and FIR wavelengths using an energy balance technique. Our version is a modification of the high- z extension (da Cunha et al. 2008) that includes the contribution from AGN emission to the SEDs (MAGPHYS+AGN; E. da Cunha et al. 2017, in preparation; S. Juneau et al. 2017, in preparation). The AGN emission is reproduced using a set of empirical templates from Mullaney et al. (2011; type 2), Richards et al. (2006), Prieto et al. (2010; QSO), and Polletta et al. (2007; Seyfert 1) as shown in Figure 2. These four templates span in a representative way the global range of known AGN SEDs; a small but representative set of templates is chosen to avoid degeneracies in the SED fitting. In our AGN sample, most of them ($> 80\%$) can find good fitting results ($0 \leq \chi^2_{\text{AGN}} \leq 3$). The contribution of the AGN template to the total IR luminosity, $\xi_{\text{AGN}} = L_{\text{dust}}^{\text{AGN}} / (L_{\text{dust}}^{\text{AGN}} + L_{\text{dust}}^{\text{SF}})$, is allowed to vary between 0 and 1 for each of the templates, and we allow the fitting code to decide which template best fits the observations while marginalizing all parameters over different contributions of the AGN component and the different AGN emission templates. Figures 3 and 4 show examples of an obscured AGN host and a QSO with a high AGN fraction. The SEDs without AGN contribution (gray lines) show the difficulty in fitting the MIR part, which can be well-fitted by the SEDs with an AGN

¹³ We adopted the Classification and Regression Trees method (Breiman et al. 1984) by scikit-learn (Pedregosa et al. 2011), and simplified the decision surface according to the contour plot. As a result, the mean accuracy score (fraction of correct predictions computed by scikit-learn) is very high (~ 0.99).

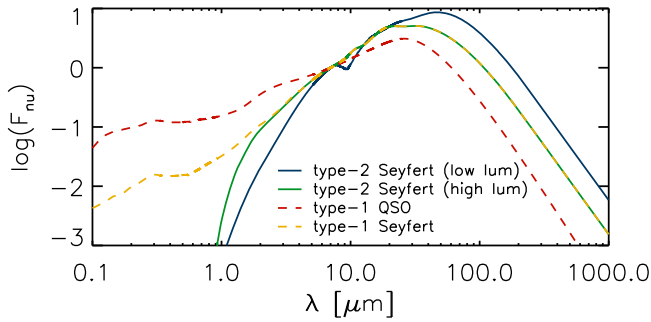


Figure 2. Four AGN empirical templates adopted in the MAGPHYS+AGN SED fitting: low-luminosity type 2 Seyfert (template = 1; Mullaney et al. 2011), high-luminosity type 2 Seyfert (template = 2; Mullaney et al. 2011), type 1 QSO (template = 4; Richards et al. 2006; Prieto et al. 2010), and type 1 Seyfert (template = 5; Polletta et al. 2007).

component (black lines, which are often plotted beneath other lines). The estimates of physical parameters of AGN hosts and the control sample of star-forming (non-AGN) galaxies are also based on our SED-fitting results.

2.3. Obscuration

In order to focus on obscured AGNs by IR selection, we use the ratio of AGN luminosity between IR and X-ray to define obscuration:

$$\frac{L_{\text{IR,AGN}}}{L_{\text{X,AGN}}}, \quad (5)$$

where $L_{\text{IR,AGN}}$ is the AGN luminosity in the IR range (3–2000 μm) and $L_{\text{X,AGN}}$ is the AGN luminosity from X-ray observations. This definition represents the bolometric luminosity inferred from the IR relative to the luminosity in the X-rays. In the upper plot in Figure 5, we adopt the 90% completeness of the X-ray luminosity as our upper limit in the X-ray luminosity to redshift plot (see Figure 7 in Marchesi et al. 2016). Therefore, we can derive the lower limit of the obscuration and select obscured AGNs as in Equation (5). Here we define obscured AGNs by $L_{\text{IR,AGN}}/L_{\text{X,AGN}} > 20$ as an arbitrary choice according to Compton-thick AGNs in Figure 5. There are 469 obscured AGNs at $z \leq 2.5$. This is another approach to obtain the obscuration besides pure X-ray spectral measurement. We also compare our selection technique with previous obscured or Compton-thick AGNs in Figure 5. This shows that our selection is reasonable, and we have a large obscured sample (red arrow) without X-ray detections.

3. SED Results

3.1. Public Catalog: MIR-selected Sources

We provide a public catalog¹⁴ for all 36,670 MIR-selected galaxies, including AGN information. In Table 2, we include ID, R.A., decl., redshift, modeling results from the preliminary MAGPHYS+AGN, and the public version of MAGPHYS, which does not include an AGN component. Note that our analyses in this paper are based on the best redshifts, including private spectroscopic redshifts from the COSMOS team; the public version here is based on the photometric redshifts in the COSMOS2015 catalog (Laigle et al. 2016). We recommend

using the MAGPHYS modeling results for objects with FLAG = 1 (20,311 out of 36,670). These are all galaxies with good-quality SED fits ($0 \leq \chi^2_{\text{AGN}} \leq 3$; $0 \leq z \leq 2.5$).

In parallel, we provide SED-fitting results, based on MAGPHYS (see Chang et al. 2015), in galaxies with available photometric redshifts (537,173 out of 1,182,108 sources) over the whole COSMOS field.

3.2. AGN Fraction and Obscuration

Figure 6 shows the stellar mass, difference in the reduced chi-square values between the SEDs with AGN and non-AGN components, and obscuration as a function of AGN bolometric fraction (AGN versus total luminosity integrated over the whole SED from the optical to FIR). The AGNs are IR selected by the color–color diagram in Section 3.1. For the control sample, we excluded IR-AGN, MAGPHYS AGN, and X-ray-selected AGN host galaxies in the star-forming galaxies hereafter. Some star-forming galaxies are bolometrically dominated by an AGN in Figure 6. It is possible that AGNs were particularly luminous in the optical, rather than in the IR or X-ray, as shown in Figure 4. In this case, we only observed the accretion disk, but not the corona or torus. Nevertheless, most of the star-forming galaxies ($\sim 96\%$) contain very low AGN contributions ($< 10\%$ bolometric AGN fraction). There are more massive AGN hosts compared to the control sample. Figure 7 also shows that AGNs are in higher-mass galaxies at all redshifts, as also found in the literature (Aird et al. 2012; Bongiorno et al. 2016). The middle panel shows the reduced chi-squared value comparison between the SED fitting without and with AGN components. There is a clear separation between AGN hosts and normal star-forming galaxies. In general, our MAGPHYS+AGN SED-fitting results work better than the standard fitting by considering the MIR contribution. The small reduced chi-squared values of high AGN fraction objects show the importance of including AGN components. The lower panel shows a slight correlation between the AGN bolometric fraction and obscuration, but it is difficult to quantify the relation due to the lower limit of obscuration of non-X-ray-detected sources. This could be due to the correlation with AGN luminosity. This implies that the emission of heavily obscured AGNs is dominated by the AGN component. The unfilled circles and lower limit symbols show that many obscured objects with a high AGN fraction are not detected in the X-ray. In our obscured IR-AGN sample, $\sim 54\%$ of them are also defined as X-ray AGNs. This is consistent with Mendez et al. (2013), who show that the fraction of X-ray AGNs that are IR-AGN selected depends on the X-ray depth. This suggests that our IR selection provides an obscured sample ($\sim 46\%$), which is hidden in the X-ray observations at the depth of the *Chandra* data in COSMOS.

3.3. Comparison with the Star-forming Main Sequence

In order to understand the star formation in AGN hosts compared to the general galaxy population, we compare our sample with the star-forming sequence (also called main sequence; e.g., Brinchmann et al. 2004; Daddi et al. 2007; Elbaz et al. 2007; Noeske et al. 2007; Chang et al. 2015; Ilbert et al. 2015; Schreiber et al. 2015). Lower star formation might imply AGN feedback, higher star formation could imply that the stellar and black hole components are both growing at the

¹⁴ <http://www.asiaa.sinica.edu.tw/~yychang/ca.html>

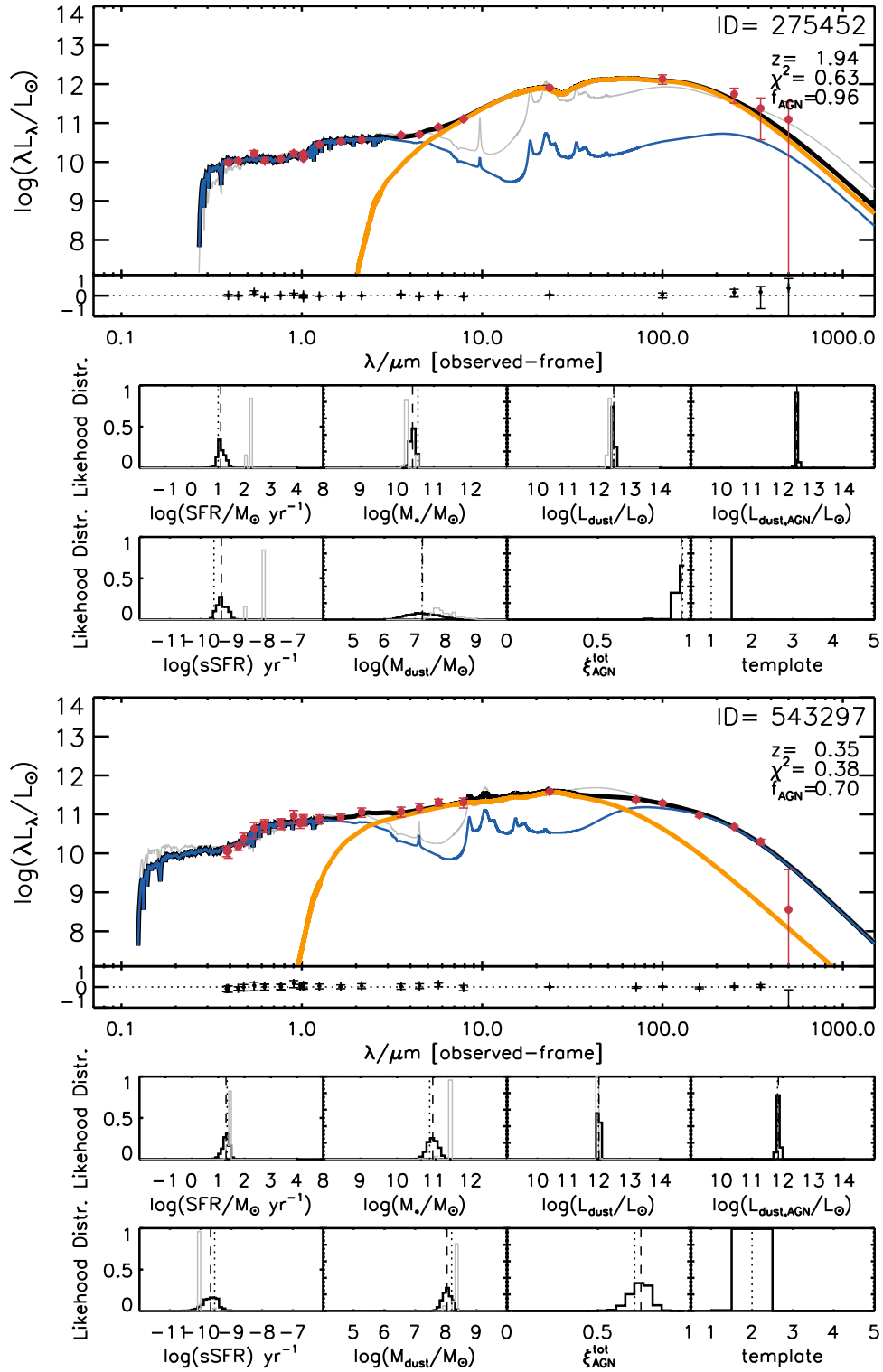


Figure 3. SED fitting with AGN component (orange line). The red points are the photometry and the black lines are the best-fitting model. The orange line is the AGN component and blue line is the star formation component. The residuals and histogram of the physical parameters are also shown for the three models. The dashed lines are the median values and the dotted lines are the best-fitting values. They gray lines show the SED-fitting results without any AGN component. As described in Figure 2, the numbers of the templates are 1 = low-luminosity type 2 Seyfert; 2 = high-luminosity type 2 Seyfert; 4 = type 1 QSO; 5 = type 1 Seyfert.

same time, and similar star formation might indicate that the AGN does not significantly affect the star formation properties.

Figure 8 shows star formation sequence plots at different redshift bins, based on our SED-fitting results. The black lines represent the star-forming galaxies, which are not classified as

IR-AGNs, MAGPHYS AGNs, or X-ray-selected AGNs in our $24 \mu\text{m}$ sample. The dotted black lines define a range of ± 0.3 dex of our star-forming sample.

We defined our own star-forming sequence, rather than using any literature to avoid biases. We fitted the median values of

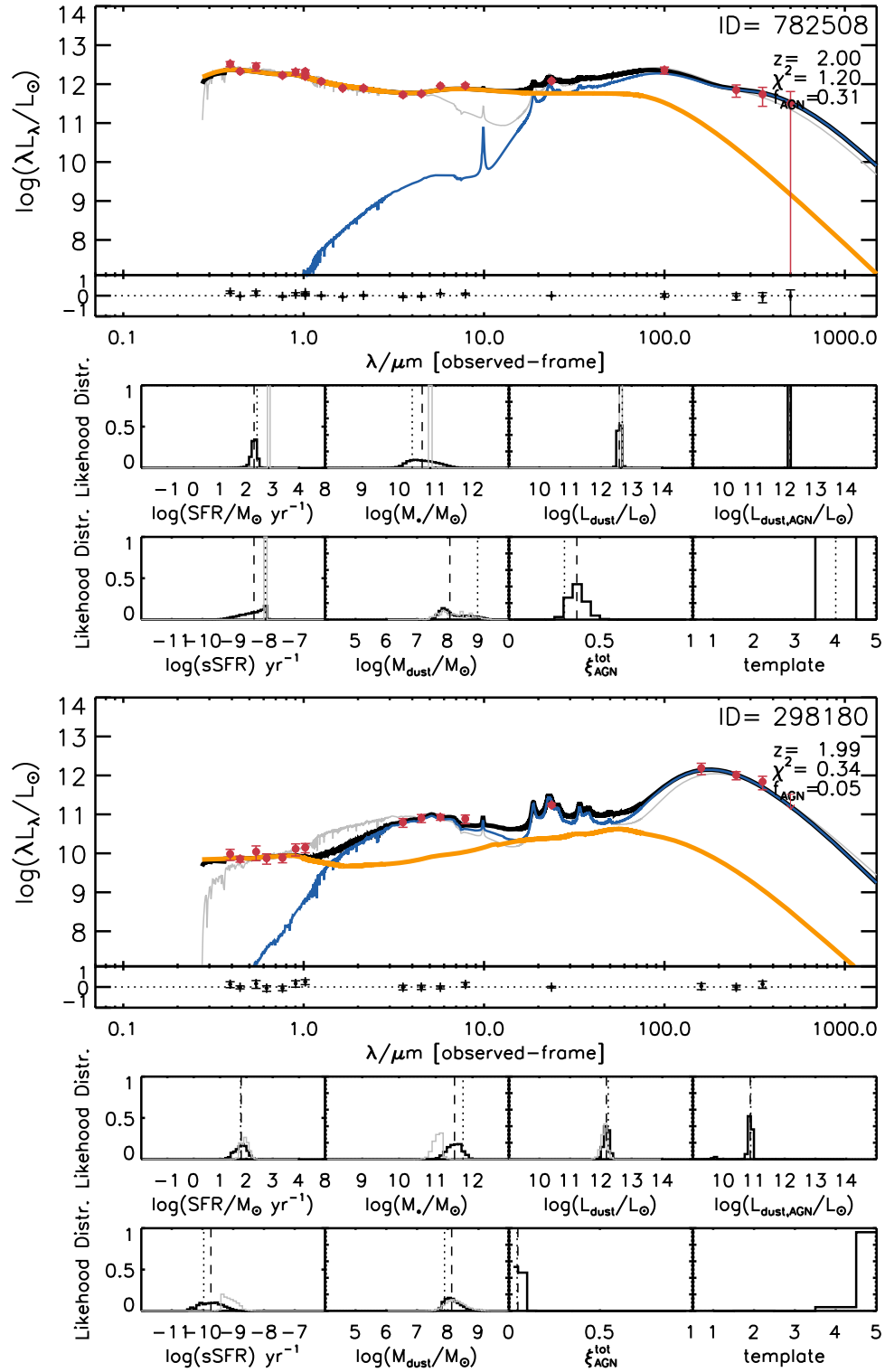


Figure 4. SED fitting with AGN component (orange line). The red points are the photometry and the black lines are the best-fitting model. The orange line is the AGN component and blue line is the star formation component. The residuals and histogram of the physical parameters are also shown for the three models. The dashed lines are the median values and the dotted lines are the best-fitting values. The gray lines show the SED-fitting results without any AGN component. As described in Figure 2, the numbers of the templates are 1 = low-luminosity type 2 Seyfert; 2 = high-luminosity type 2 Seyfert; 4 = type 1 QSO; 5 = type 1 Seyfert.

the star-forming sequence with a power law and find

$$\log \text{SFR} / (M_{\odot} \text{ yr}^{-1}) = a \log M_{*} / (M_{\odot}) - b, \quad (6)$$

where a and b are shown in Table 3. The red lines represent the IR-AGN sample, and the orange lines show the obscured

IR-AGN sample, which are defined by our MIR color-color plot and obscuration as described in Section 2. The green lines show the X-ray-selected AGNs from *Chandra* Legacy Survey with L_X (2–10 keV) $> 10^{42} \text{ erg s}^{-1}$. Figure 9 shows the specific star formation rate (sSFR) as a function of redshift for two

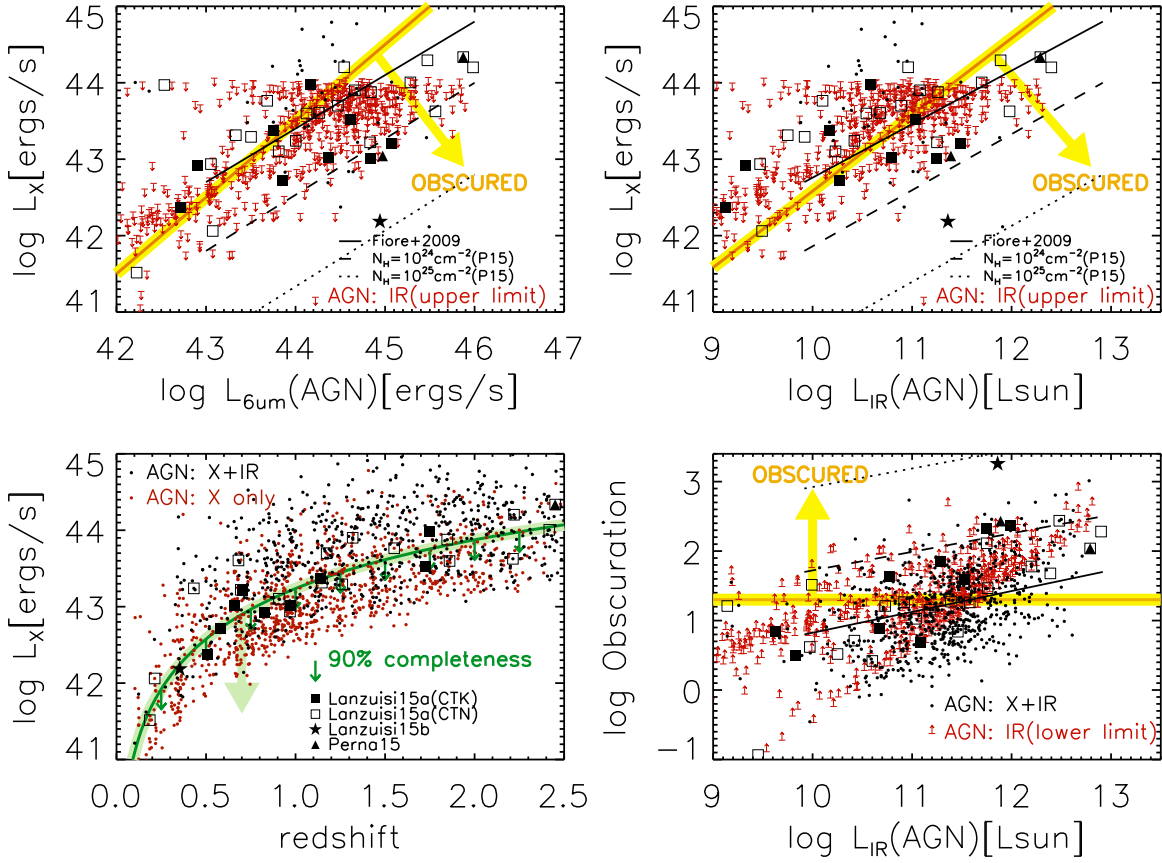


Figure 5. Obscured AGN selection. Upper left: X-ray luminosity vs. $6\mu m$ luminosity from the AGN component. This plot is comparable to that in Fiore et al. (2009), Lanzuisi et al. (2015a, 2015b), and Perna et al. (2015). The red arrows are those sources where the upper limit has been calculated using the 90% completeness threshold for X-ray detection (green line) illustrated in the lower-left panel. Upper right: X-ray luminosity vs. IR luminosity from the AGN component. Lower left: X-ray luminosity vs. redshift plot. Here we define the upper limit (green line and arrows) of the X-ray luminosity (90% completeness) for IR-selected AGNs. The red points represent AGNs that are only selected by X-ray, and the black points are selected both by X-ray and IR. Lower right: ratio between IR luminosity and X-ray luminosity from the AGN vs. IR luminosity plot. We choose $L_{IR,AGN}/L_{X,AGN} > 20$ as IR-obscured AGNs (yellow and orange lines).

stellar mass bins. We find that our IR-selected AGN hosts are not significantly or slightly above the star-forming sequence at $z < 1.5$. In Figures 8 and 9, the most massive obscured IR-AGN hosts could be above the main sequence at all redshifts, but most ($>70\%$) obscured IR-AGN hosts at $10.5 < \log M_*/M_\odot < 11$ are below the star-forming sequence at $z > 1.5$. In general, X-ray-selected AGN hosts are close to the star-forming sequence at all redshift and stellar mass bins, which implies that AGN host galaxies by both IR and X-ray selections are mostly on the main sequence.

3.4. Additional Parameter Constraints from SEDs

In Figures 10 and 11, we show some key physical properties of their stacked likelihood distributions from SED fitting for mass-matched sample, according to the stellar mass distribution of star-forming galaxies (control sample). As discussed in Figures 8 and 9, we see slight differences between the SFRs and sSFRs. As a result, the mass-weighted ages of AGNs are younger than star-forming galaxies at $z \sim 1$ but older at $z \sim 2$. The AGN fraction and luminosity of IR-AGNs are higher than X-ray-selected AGNs and normal galaxies at all redshifts. In particular, the obscured IR-AGN sample shows the highest AGN luminosity. It is clear to see that the AGN IR fraction and AGN luminosity of the star-forming galaxies are significantly different from AGNs.

4. Morphological Analysis

In this section, we will show the influence of obscuration and AGN fraction on morphology. We use *HST*/ACS *I*-band images to study a sample at $0.5 < z < 1.5$ and $\log M_*/M_\odot > 10.5$. We focus on obscured IR-AGN hosts with $L_{IR,AGN}/L_{X,AGN} > 20$ as defined in Section 2 and discussed in Section 3 (orange lines in Figures 8–11), which ensures that the optical imaging of the hosts is not affected by AGNs.

4.1. GALFIT

We used both single-Sérsic profile and Sérsic+PSF profile measured by GALFIT (Peng et al. 2002, 2010). As described by Chang et al. (2017), a PSF component is a negligible term, so we focus on single-Sérsic fitting results to compare with star-forming galaxies. In Figure 12, we find that there is a slight trend between AGN fraction and radius/Sérsic index. AGN hosts seem to be more compact (smaller in radius and larger in Sérsic index) while the AGN fraction is higher. Moreover, AGN hosts are also more compact than normal star-forming galaxies. This is consistent with our recent finding about compact AGN hosts in Chang et al. (2017), which suggested a possible indication of compaction of AGN hosts and that a vast majority of obscured AGNs might reside in galaxies undergoing dynamical compaction. We also check the relation between obscuration and GALFIT parameters in Figure 12 and

Table 2
MAGPHYS+AGN Output Catalog in the COSMOS Field

Column Name	Format	Unit	Column Description
NUMBER	LONG	...	COSMOS2015 index
ALPHA_J2000	DOUBLE	deg	J2000 R.A. [deg] from COSMOS2015
DELTA_J2000	DOUBLE	deg	J2000 Decl. [deg] from COSMOS2015
PHOTO_Z	DOUBLE	...	photometric redshift from COSMOS2015
TEMPLATE	INT	...	AGN template; 1: low lum type 2; 2:high lum type 2; 4: QSO type 1; 5: Seyfert type 1
MASS_2_5_AGN	FLOAT	$\log M_{\odot}$	log stellar mass (2.5th percentile) [MAGPHYS+AGN]
MASS_16_AGN	FLOAT	$\log M_{\odot}$	log stellar mass (16th percentile) [MAGPHYS+AGN]
MASS_50_AGN	FLOAT	$\log M_{\odot}$	log stellar mass (50th percentile) [MAGPHYS+AGN]
MASS_84_AGN	FLOAT	$\log M_{\odot}$	log stellar mass (84th percentile) [MAGPHYS+AGN]
MASS_97_5_AGN	FLOAT	$\log M_{\odot}$	log stellar mass (97.5th percentile) [MAGPHYS+AGN]
SFR_2_5_AGN	FLOAT	$\log M_{\odot} \text{ yr}^{-1}$	log SFR (2.5th percentile) [MAGPHYS+AGN]
SFR_16_AGN	FLOAT	$\log M_{\odot} \text{ yr}^{-1}$	log SFR (16th percentile) [MAGPHYS+AGN]
SFR_50_AGN	FLOAT	$\log M_{\odot} \text{ yr}^{-1}$	log SFR (50th percentile) [MAGPHYS+AGN]
SFR_84_AGN	FLOAT	$\log M_{\odot} \text{ yr}^{-1}$	log SFR (84th percentile) [MAGPHYS+AGN]
SFR_97_5_AGN	FLOAT	$\log M_{\odot} \text{ yr}^{-1}$	log SFR (97.5th percentile) [MAGPHYS+AGN]
AV_2_5_AGN	FLOAT	...	dust attenuation parameter (2.5th percentile) [MAGPHYS+AGN]
AV_16_AGN	FLOAT	...	dust attenuation parameter (16th percentile) [MAGPHYS+AGN]
AV_50_AGN	FLOAT	...	dust attenuation parameter (50th percentile) [MAGPHYS+AGN]
AV_84_AGN	FLOAT	...	dust attenuation parameter (84th percentile) [MAGPHYS+AGN]
AV_97_5_AGN	FLOAT	...	dust attenuation parameter (97.5th percentile) [MAGPHYS+AGN]
AGNF_2_5_AGN	FLOAT	...	AGN IR fraction (2.5th percentile) [MAGPHYS+AGN]
AGNF_16_AGN	FLOAT	...	AGN IR fraction (16th percentile) [MAGPHYS+AGN]
AGNF_50_AGN	FLOAT	...	AGN IR fraction (50th percentile) [MAGPHYS+AGN]
AGNF_84_AGN	FLOAT	...	AGN IR fraction (84th percentile) [MAGPHYS+AGN]
AGNF_97_5_AGN	FLOAT	...	AGN IR fraction (97.5th percentile) [MAGPHYS+AGN]
LDUST_2_5_AGN	FLOAT	$\log L_{\odot}$	log dust luminosity (2.5th percentile) [MAGPHYS+AGN]
LDUST_16_AGN	FLOAT	$\log L_{\odot}$	log dust luminosity (16th percentile) [MAGPHYS+AGN]
LDUST_50_AGN	FLOAT	$\log L_{\odot}$	log dust luminosity (50th percentile) [MAGPHYS+AGN]
LDUST_84_AGN	FLOAT	$\log L_{\odot}$	log dust luminosity (84th percentile) [MAGPHYS+AGN]
LDUST_97_5_AGN	FLOAT	$\log L_{\odot}$	log dust luminosity (97.5th percentile) [MAGPHYS+AGN]
LDUSTAGN_2_5_AGN	FLOAT	$\log L_{\odot}$	log dust AGN luminosity (2.5th percentile) [MAGPHYS+AGN]
LDUSTAGN_16_AGN	FLOAT	$\log L_{\odot}$	log dust AGN luminosity (16th percentile) [MAGPHYS+AGN]
LDUSTAGN_50_AGN	FLOAT	$\log L_{\odot}$	log dust AGN luminosity (50th percentile) [MAGPHYS+AGN]
LDUSTAGN_84_AGN	FLOAT	$\log L_{\odot}$	log dust AGN luminosity (84th percentile) [MAGPHYS+AGN]
LDUSTAGN_97_5_AGN	FLOAT	$\log L_{\odot}$	log dust AGN luminosity (97.5th percentile) [MAGPHYS+AGN]
MASS_2_5_0	FLOAT	$\log M_{\odot}$	log stellar mass (2.5th percentile) [MAGPHYS]
MASS_16_0	FLOAT	$\log M_{\odot}$	log stellar mass (16th percentile) [MAGPHYS]
MASS_50_0	FLOAT	$\log M_{\odot}$	log stellar mass (50th percentile) [MAGPHYS]
MASS_84_0	FLOAT	$\log M_{\odot}$	log stellar mass (84th percentile) [MAGPHYS]
MASS_97_5_0	FLOAT	$\log M_{\odot}$	log stellar mass (97.5th percentile) [MAGPHYS]
SFR_2_5_0	FLOAT	$\log M_{\odot} \text{ yr}^{-1}$	log SFR (2.5th percentile) [MAGPHYS]
SFR_16_0	FLOAT	$\log M_{\odot} \text{ yr}^{-1}$	log SFR (16th percentile) [MAGPHYS]
SFR_50_0	FLOAT	$\log M_{\odot} \text{ yr}^{-1}$	log SFR (50th percentile) [MAGPHYS]
SFR_84_0	FLOAT	$\log M_{\odot} \text{ yr}^{-1}$	log SFR (84th percentile) [MAGPHYS]
SFR_97_5_0	FLOAT	$\log M_{\odot} \text{ yr}^{-1}$	log SFR (97.5th percentile) [MAGPHYS]
AV_2_5_0	FLOAT	...	dust attenuation parameter (2.5th percentile) [MAGPHYS]
AV_16_0	FLOAT	...	dust attenuation parameter (16th percentile) [MAGPHYS]
AV_50_0	FLOAT	...	dust attenuation parameter (50th percentile) [MAGPHYS]
AV_84_0	FLOAT	...	dust attenuation parameter (84th percentile) [MAGPHYS]
AV_97_5_0	FLOAT	...	dust attenuation parameter (97.5th percentile) [MAGPHYS]
LDUST_2_5_0	FLOAT	$\log L_{\odot}$	log dust luminosity (2.5th percentile) [MAGPHYS]
LDUST_16_0	FLOAT	$\log L_{\odot}$	log dust luminosity (16th percentile) [MAGPHYS]
LDUST_50_0	FLOAT	$\log L_{\odot}$	log dust luminosity (50th percentile) [MAGPHYS]
LDUST_84_0	FLOAT	$\log L_{\odot}$	log dust luminosity (84th percentile) [MAGPHYS]
LDUST_97_5_0	FLOAT	$\log L_{\odot}$	log dust luminosity (97.5th percentile) [MAGPHYS]
FLAG	INT	...	flag (1 = good fits; 0 = others)

Note. We recommend using the MAGPHYS modeling results for objects with FLAG = 1. These are all $0 \leq z \leq 2.5$ galaxies with good-quality SED fits ($0 \leq \chi^2_{\text{AGN}} \leq 3$).

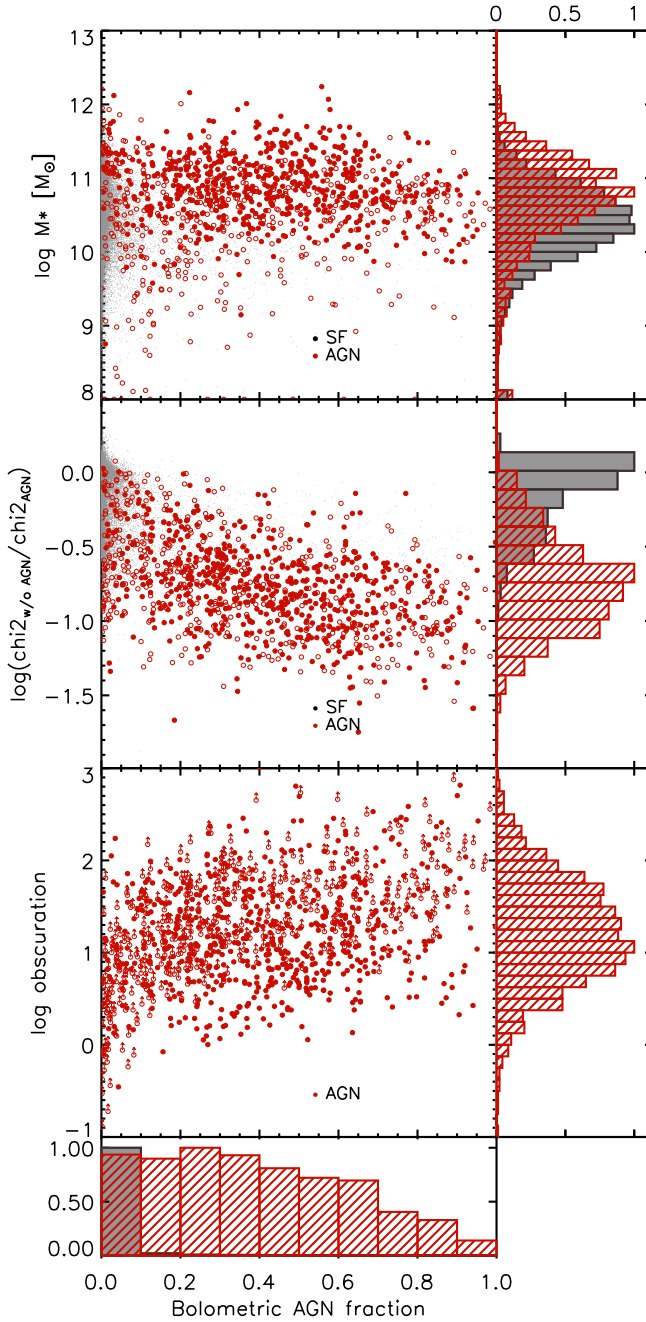


Figure 6. Upper panel: AGN bolometric fraction vs. stellar mass plot for normal star-forming galaxies (gray) and IR-selected AGNs (red). The unfilled circles represent AGNs without X-ray detection (L_X (2–10 keV) $< 10^{42}$ erg s $^{-1}$). Middle panel: AGN bolometric fraction vs the ratio of the chi-squared value plot. The ratio represents the chi-squared values between the SED-fitting results without and with AGN templates. The AGN templates improve the SED fitting, especially for high AGN fraction objects. Lower panel: AGN bolometric fraction vs. obscuration plot. For non-X-ray-detected sources, we show the lower limit of the obscuration (red arrow). There is a slight correlation between the AGN fraction and obscuration.

find that there is almost no correlation (Pearson correlation coefficient < 0.1).

In Figure 13, we plot the radius and Sérsic index as functions of bolometric AGN fraction, $\log r = -(0.61 \pm 0.11)f + (0.53 \pm 0.05)$ and $n = (1.04 \pm 0.41)f + (1.10 \pm 0.16)$, where r is the radius in kpc, n is the Sérsic index, and f is the bolometric AGN fraction. According to these relations, a 20% AGN contribution corresponds to a radius decrease of

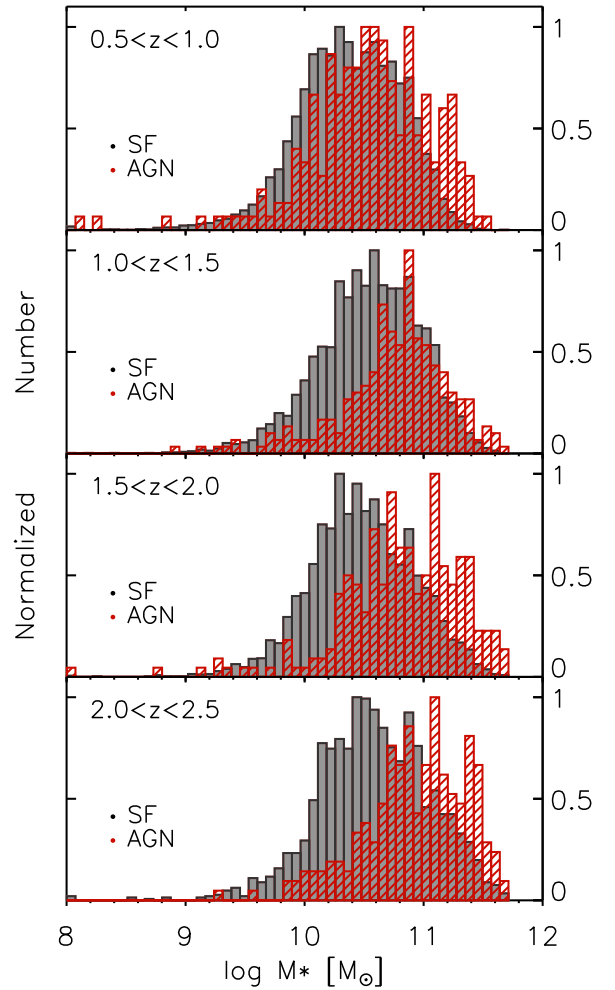


Figure 7. Mass distribution in different redshift bins. AGNs are in massive galaxies at all redshift bins.

24% and a Sérsic index increase of 18%, and a 50% AGN contribution corresponds to a radius decrease of 50% and a Sérsic index increase of 47%.

4.2. Nonparametric Morphology Method

We used the Zurich Structure & Morphology catalog (Sargent et al. 2007; Scarlata et al. 2007) in the COSMOS field to investigate the relation between nonparametric methods and AGN fraction/obscuration in the upper plot of Figure 14. The four nonparametric measures are individual estimators of galaxy structures: concentration C , asymmetry A , Gini coefficient G , and second-order moment of the brightest 20% of galaxy pixels M_{20} (e.g., Abraham et al. 2003; Conselice 2003; Lotz et al. 2004). We also compared with the Cassata et al. (2007) catalog in the lower plot. It is clear that AGN host galaxies (pink) are significantly different from star-forming galaxies (blue/gray). In general, AGN hosts are more compact and asymmetric compared with normal galaxies. AGN hosts also have a slightly higher Gini coefficient and lower M_{20} than star-forming galaxies but the majority of them are still not merger-like in the Gini- M_{20} plot as shown in Figure 15. The lines here are from Lotz et al. (2008), which was adopted for $0.2 < z < 1.2$ Extended Groth Strip galaxies. The merger fraction might evolve over redshifts (Lotz et al. 2011; Peth et al. 2016), but our control sample also provides a fair

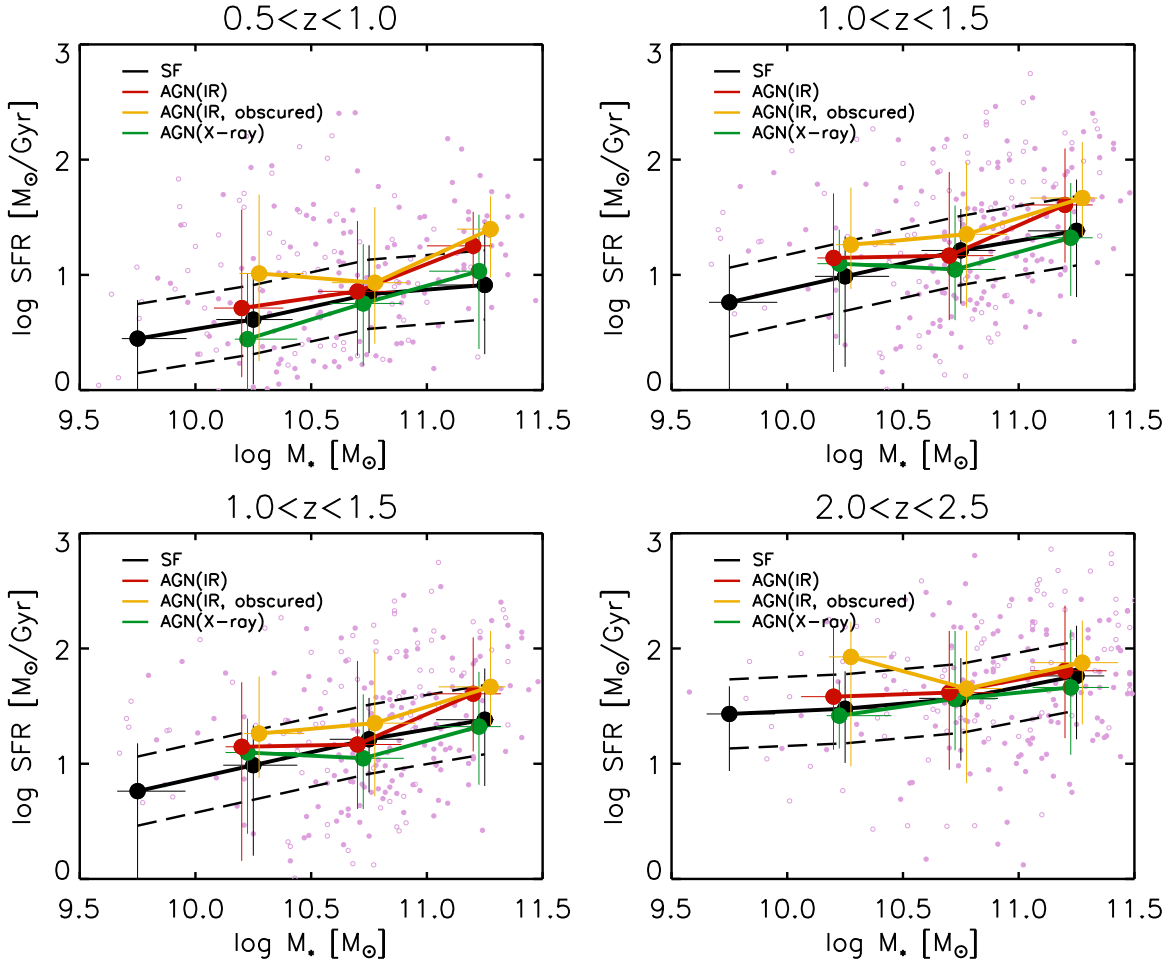


Figure 8. Star-forming sequence (main sequence) plot. The black solid and dashed lines show the star-forming sequence. Here we show the median and the 84%–16% values of IR-AGN hosts (red), obscured IR-AGN hosts (orange), X-ray AGN hosts (green), and star-forming galaxies (black). The plum dots show individual IR-AGN hosts. The open circles represent AGNs without X-ray detection. Obscured AGNs lie within or slightly above the star-forming sequence.

comparison. Both catalogs show that the AGN fraction follows the directions of the offset of structural parameters, that is, the AGN fraction is higher while the hosts are more compact, asymmetric, and bulgier (higher Gini and lower M_{20}). Obscuration has no strong correlation, except that obscured AGN hosts seem to be more symmetric. This suggests that the compactness is not sensitive to obscuration in our sample.

Figures 16 and 17 show the comparison of nonparametric measures in the mass versus SFR plot at different redshift bins. The Kolmogorov–Smirnov (K–S) tests suggest that the morphology parameters of AGN hosts and normal star-forming galaxies are indistinguishable in many bins, but still show significant differences ($P_{K-S} < 0.05$) in several bins, which we highlight with thick green boxes. Though the sample size is small in each bin, this implies that obscured AGN hosts do not necessarily have similar structures to normal galaxies. It might be also linked to our previous finding of compact AGN host galaxies, and provide possible constraints on future scenarios.

4.3. Visual Classification

We separated all AGNs (IR and X-ray selected) and randomly selected 1000 star-forming galaxies at $z < 1.5$ and $\log M_*/M_\odot > 10$, which we classify using four classes: disk, spheroid, irregular/merger, and point source (Figure 18). These classes are mutually exclusive, so the classification represents

the dominant morphology. All of the objects are examined by six classifiers (Y.-Y.C., Y.T., C.-F.L., J.-J.T., W.H.-W., N.F.). Following previous subsections, we only focus on the obscured IR-AGNs and the control sample at $0.5 < z < 1.5$ and $\log M_*/M_\odot > 10.5$ as in our earlier work (Chang et al. 2017). Figure 19 shows the classification results. The error bars in each class represents the 68.3% (1σ) confidence limits, derived using the method in Cameron (2011), which considers the estimation of the confidence intervals for a binomial population with a Bayesian approach. This shows that the spheroid fraction of AGNs ($\sim 30\%$) is higher than that of star-forming galaxies ($\sim 10\%$). The merger fraction of obscured AGNs ($\sim 30\%$) is lower than that of the control sample ($\sim 40\%$). The sample size is limited to make small bins of redshift and stellar mass. Nevertheless, the results are consistent for objects at $0.5 < z < 1.5$ and $\log M_*/M_\odot > 10.5$.

In the upper panel of Figure 20, we find a correlation between the total IR luminosity of obscured AGNs and the merger fraction. For the most luminous AGNs ($\log(L_{\text{IR}}/L_\odot) \sim 12.5$), the merger fraction can reach up to a fraction of 0.5. Moreover, the increase of the merger fraction occurs for the whole star-forming population, not only for AGN hosts. The lower panel of Figure 20 shows that, from our SED decomposition, merger fraction has no dependence on the AGN IR luminosity but does have dependence on the star-forming IR luminosity. This implies that the IR luminosity of star formation, rather than the IR

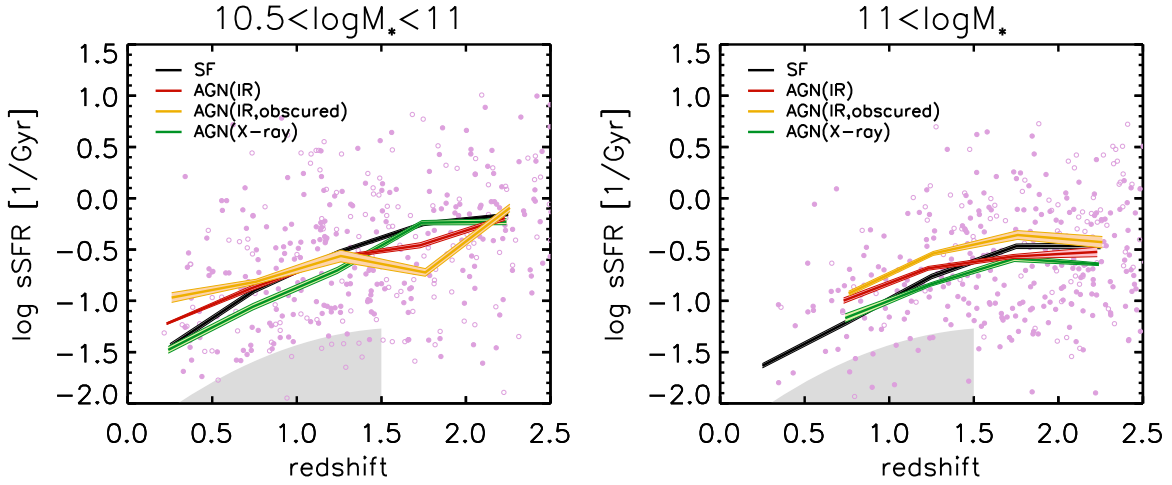


Figure 9. Specific SFR (sSFR) as a function of redshift in two different stellar mass bins. Here we show the median value of IR-AGN hosts (red), obscured IR-AGN hosts (orange), X-ray AGN hosts (green), and star-forming galaxies (black). The error bars are from bootstrapping. The plum dots show individual IR-AGN hosts. The open circles represent AGNs without X-ray detection. The shading region is the lower limit adopted from Ilbert et al. (2015). The sSFR of obscured AGNs are similar to or slightly larger than normal galaxies.

luminosity of AGNs, can be responsible for the disturbed features. In general, our obscured AGN hosts have no strong disturbed features, which imply that the merger features are dominated by the total luminosity. It might be more difficult to distinguish merger features of faint sources. Nevertheless, the increased merger rate only happens to the most luminous galaxies for both normal and AGN host galaxies.

5. Discussion

5.1. How Does Star Formation Regulate AGN Activity?

In general, the offsets in the star-forming sequence between AGN hosts and star-forming galaxies are not significant. At $z < 1.5$, our obscured AGN hosts are slightly above the main sequence, which seems to be consistent with previous findings of SFR enhancement in MIR-selected galaxies (Ellison et al. 2016; Azadi et al. 2017). A possible explanation is that an abundant gas supply triggers enhanced star formation in an obscured AGN phase. Moreover, the sSFRs of massive obscured AGN hosts are also slightly higher than in the control sample up to $z \sim 2.5$. However, the lack of star-bursting host galaxies (i.e., galaxies above the star-forming sequence) in the obscured sample at $10.5 < \log M_*/M_\odot < 11$ leads to a low sSFR at $z > 1.5$. With the mass-matched sample in Section 3.4, we can see there is little difference in the star formation-heated IR luminosity among the AGNs and the control sample. Overall, the star-forming component of obscured AGN host galaxies have slightly higher SFRs, sSFRs, and IR luminosities, consistent with the result in Juneau et al. (2013).

Besides the (specific) SFR, other physical properties from SED fitting are slightly different (low significance level by K-S test) between AGN hosts and normal galaxies as shown in Section 3.4. In particular, the stellar mass-weighted ages, attenuation, and IR parameters of our obscured samples are significantly different ($P_{K-S} < 0.05$) from normal star-forming galaxies. It is natural to see higher IR luminosity and AGN fraction for our MIR-selected IR-AGNs. At lower redshifts, obscured AGN hosts seem slightly younger and more dust attenuated than star-forming galaxies. Owing to the small offsets, it is difficult to rule out or confirm a model in which

Table 3
Fitting Parameters of the SFR to Stellar Mass Plot (Main Sequence; See also Figure 8) in Equation (6)

Redshift	a	b
Star-forming Galaxies		
$0.5 < z < 1.0$	0.34 ± 0.02	-2.86 ± 0.24
$1.0 < z < 1.5$	0.42 ± 0.02	-3.30 ± 0.24
$1.5 < z < 2.0$	0.34 ± 0.02	-2.16 ± 0.26
$2.0 < z < 2.5$	0.22 ± 0.04	-0.80 ± 0.45
IR-AGN Hosts		
$0.5 < z < 1.0$	0.53 ± 0.18	-4.76 ± 1.93
$1.0 < z < 1.5$	0.50 ± 0.18	-4.08 ± 1.93
$1.5 < z < 2.0$	0.47 ± 0.13	-3.66 ± 1.36
$2.0 < z < 2.5$	0.25 ± 0.19	-0.96 ± 2.01
IR-AGN Hosts (Obscured)		
$0.5 < z < 1.0$	0.35 ± 0.24	-2.68 ± 2.64
$1.0 < z < 1.5$	0.42 ± 0.18	-3.08 ± 1.91
$1.5 < z < 2.0$	0.64 ± 0.19	-5.53 ± 2.08
$2.0 < z < 2.5$	0.00 ± 0.28	1.76 ± 3.08
X-ray AGN Hosts		
$0.5 < z < 1.0$	0.59 ± 0.10	-5.57 ± 1.08
$1.0 < z < 1.5$	0.27 ± 0.08	-1.79 ± 0.91
$1.5 < z < 2.0$	0.40 ± 0.09	-2.82 ± 0.95
$2.0 < z < 2.5$	0.24 ± 0.14	-0.99 ± 1.48

Note. The uncertainties are estimated by bootstrapping ($N = 1000$).

mergers fuel rapid starburst and a phase of obscured black hole growth, followed by an unobscured phase (e.g., Sanders et al. 1988; see Alexander & Hickox 2012 for a review) due to the small offsets. However, at $z > 1.5$, the stellar mass-weighted ages of obscured AGN hosts are significantly different from and larger than those of the control sample. It might be related to the previous results on the lifetime of strongly clustered obscured AGNs (Hickox et al. 2011; DiPompeo et al. 2014; Toba et al. 2017), but we still need further constraints on ages since ages derived from broadband photometry are highly

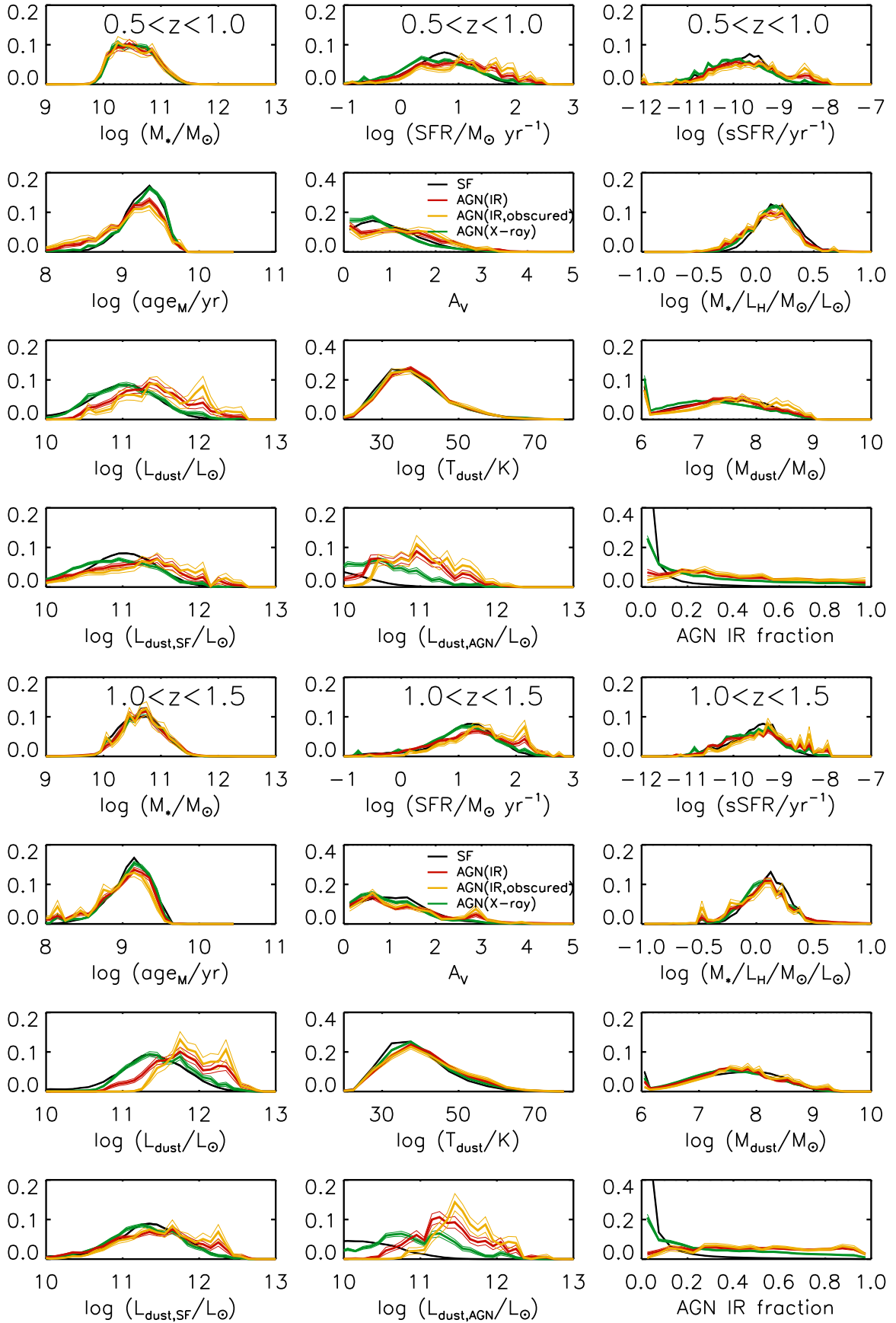


Figure 10. Normalized stacked likelihood distributions of the different physical parameters of mass-matched star-forming galaxies (black line), IR-AGN hosts (red), obscured IR-AGN hosts (orange), and X-ray AGN hosts (green line) at $0.5 < z < 1.0$ and $1.0 < z < 1.5$. The thin lines are the uncertainties estimated by bootstrapping. See da Cunha et al. (2015) for more details about these physical properties.

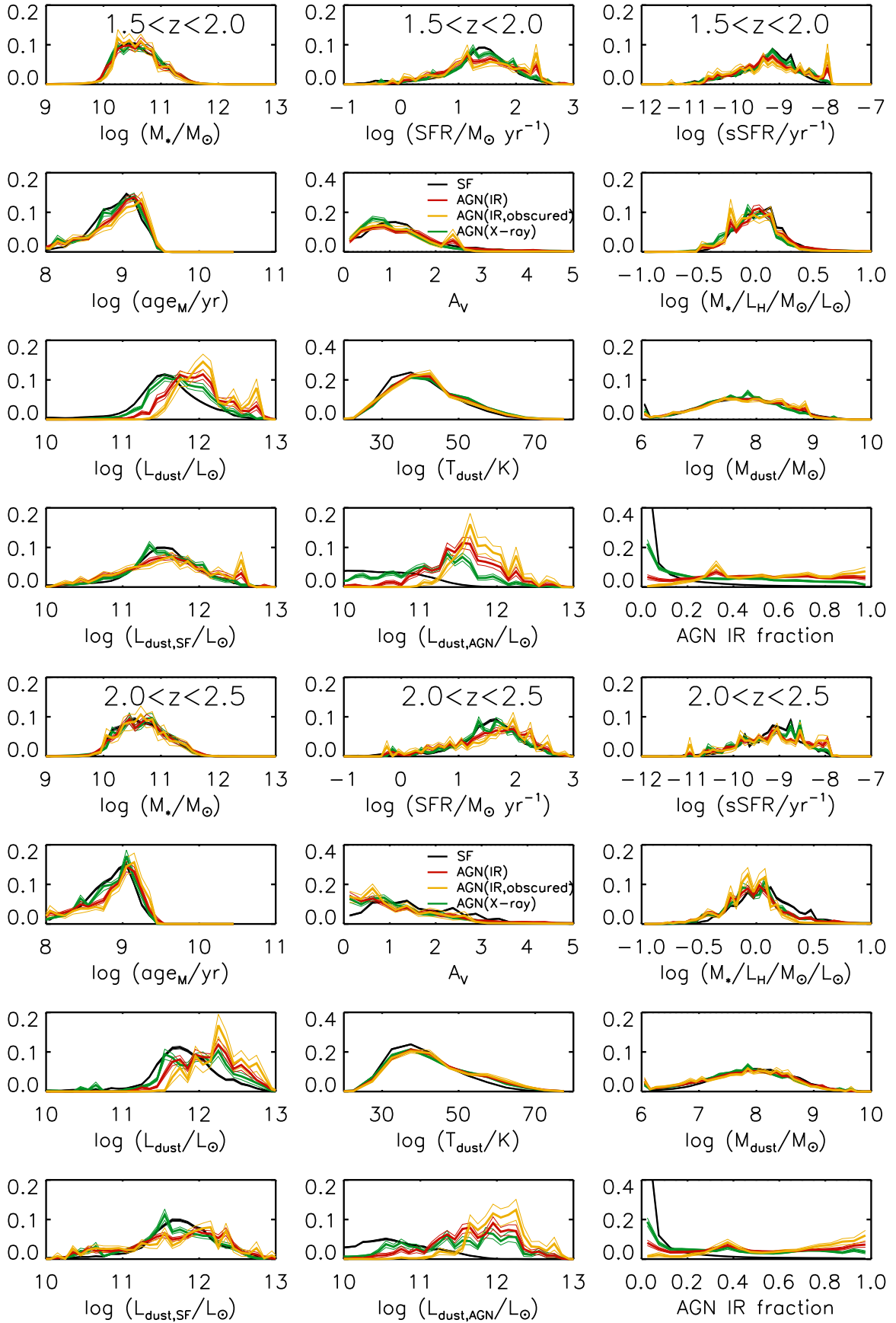


Figure 11. Normalized stacked likelihood distributions of the different physical parameters of mass-matched star-forming galaxies (black line), IR-AGN hosts (red), obscured IR-AGN hosts (orange), and X-ray AGN hosts (green line) at $1.5 < z < 2.0$ and $2.0 < z < 2.5$. The thin lines are the uncertainties estimated by bootstrapping. See da Cunha et al. (2015) for more details about these physical properties.

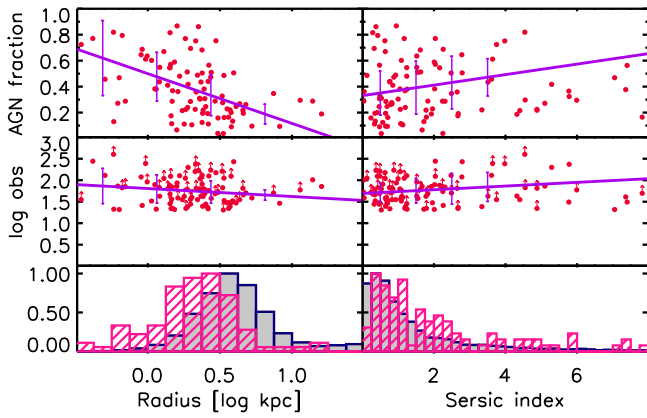


Figure 12. Radius and Sérsic index of single-Sérsic fitting from GALFIT results at $0.5 < z < 1.5$ and $\log M_*/M_\odot > 10.5$. Here we compare the GALFIT parameters with bolometric AGN fraction and obscuration for obscured IR-AGN hosts (red). We also show histograms of obscured IR-AGN hosts (pink) and normal star-forming galaxies (blue/gray). The purple lines show the results of linear fitting, and the error bars represent the standard deviation in each bin. We only consider detected sources in the linear fitting for obscuration.

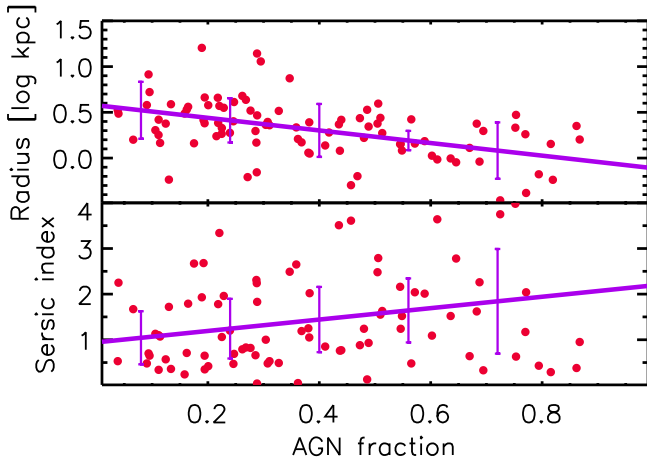


Figure 13. Radius and Sérsic index as functions of bolometric AGN fraction. The purple lines show the results of linear fitting and the error bars represent the standard deviation in each bin. According to the linear correlation (purple line), a 20% AGN contribution corresponds to a radius decrease of 24% and a Sérsic index increase of 18%, and a 50% AGN contribution corresponds to a radius decrease of 50% and a Sérsic index increase of 47%.

uncertain. Moreover, our SFRs take the average star formation over the last 10^8 years while AGNs can be luminous on scales as low as 10^5 years. It might be a reason why it is difficult to see a significant difference in the main-sequence location between AGNs and normal galaxies.

5.2. Are Obscured IR-AGNs Different from X-Ray-selected AGNs?

Compton-thick AGNs are hidden by extreme column densities ($N_H \gtrsim 10^{24} \text{ cm}^{-2}$) because neutral gas can absorb X-ray photons. They are believed to provide an important contribution to the overall cosmic energy budget as well as constraints on the co-evolution of AGN and galaxies. However, the identification of heavily obscured AGNs is difficult, and a significant fraction of AGN are hidden by Compton-thick obscuration (e.g., Ueda et al. 2003; Treister et al. 2009). Our AGN sample is based on an IR color-color selection, rather than the widely used X-ray selection, and we select obscured

AGNs using the ratio between IR and X-ray luminosity. It provides a sample of obscured AGNs that is complementary to a Compton-thick AGN sample selected purely by X-ray observations.

Suh et al. (2017) found that X-ray type 2 AGN hosts have similar SFRs to those of normal star-forming galaxies. In this paper, we confirmed this result with our X-ray-selected sample, and showed that IR-selected AGN hosts are not significantly different from or slightly above the star-forming sequence. Besides, the distribution of physical parameters, such as stellar mass-weighted age, attenuation, and IR properties, seems to be different for IR-selected AGNs, while the distribution of X-ray-selected AGNs is close to that of normal galaxies. The differences between AGN types might be interpreted as different phases in the evolutionary sequence (Hopkins et al. 2008). Hickox et al. (2009) showed that X-ray-selected AGNs are preferentially found in the “green valley” and clustered similarly to normal galaxies, while IR-selected AGNs reside in slightly bluer, slightly less luminous galaxies than X-ray AGNs, and are weakly clustered. Moreover, Brusa et al. (2010) discovered an obscured QSO at high- z caught in a transition stage from being starburst dominated to AGN dominated. Our results from an MIR-selection sample imply that obscured AGNs can be in a different evolutionary stage from X-ray-selected AGNs.

According to the Gini- M_{20} plot in Figure 15 and visual classification in Figure 20, we did not find a high merger rate in the whole obscured AGN sample. However, Figure 20 showed an increasing merger fraction with IR luminosity, which is consistent with the model prediction of Hickox et al. (2014) and many previous observational results (e.g., Zamojski et al. 2011; Kocevski et al. 2015; Lanzuisi et al. 2015a; Fan et al. 2016). The high merger fraction of the most luminous obscured AGN hosts is consistent with recent results from *HST*/WFC3 imaging (Kocevski et al. 2015; D12), which suggested that Compton-thick AGNs are in a different phase of obscured supermassive black hole growth following a merger/interaction event. The low dependence of merger fraction on the IR luminosity from the AGN component implies that the interaction event is more relevant to the total or star-forming IR luminosity, rather than the AGN IR luminosity. Moreover, we also find a correlation between merger fraction and total IR luminosity for normal galaxies. It is interesting that star-forming galaxies are more likely to be in a merger than AGN hosts at $\log(L_{\text{IR}}/L_\odot) > 11$. A possible explanation is that our obscured AGNs are selected by IR with intermediate luminosity. If we consider their compact features, which will be discussed in the next subsection together, it may suggest that these obscured AGN hosts are in a special evolutionary stage. This finding can provide morphological constraints for future studies on different types of AGN hosts in galaxy evolution (e.g., Alexander & Hickox 2012; Goulding et al. 2014). Our results also suggest that the whole obscured sample, including non-X-ray-detected sources, shows no stronger disturbed features compared to normal galaxies, and the increased merger fraction may only occur in the most luminous galaxies.

5.3. Are AGNs Triggered by Compaction?

In terms of optical morphological interpretation, obscured AGNs offer an advantage in the avoidance of the PSF contribution to the optical image. This is consistent with earlier X-ray results without consideration of AGN contribution

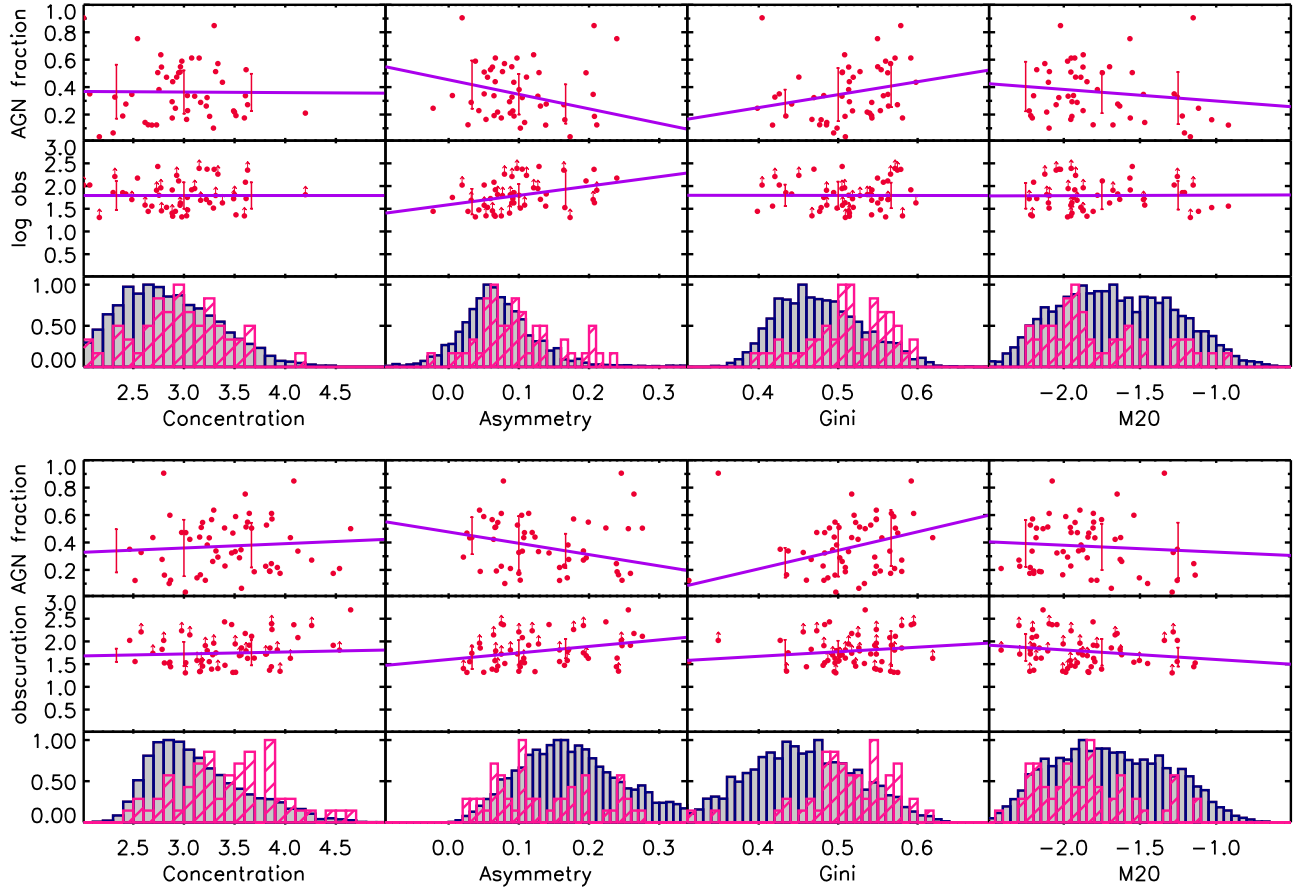


Figure 14. Morphology parameters: concentration, asymmetry, Gini, and M_{20} at $0.5 < z < 1.5$ and $\log M_*/M_\odot > 10.5$. Here we compare the morphological parameters with the bolometric AGN fraction and obscuration for obscured IR-AGN hosts (red). We also show the histograms of obscured IR-AGN hosts (pink) and normal star-forming galaxies (blue/gray). The upper plot shows the value from the Zurich Structure & Morphology catalog (Sargent et al. 2007; Scarlata et al. 2007), and the lower plot shows the value from Cassata et al. (2007) catalog. The purple lines show the results of linear fitting and the error bars represent the standard deviation in each bin. We only consider detected sources in the linear fitting for obscuration. In general, AGN hosts are more compact and asymmetric compared with normal galaxies. AGN hosts also have a slightly higher Gini coefficient and lower M_{20} than star-forming galaxies.

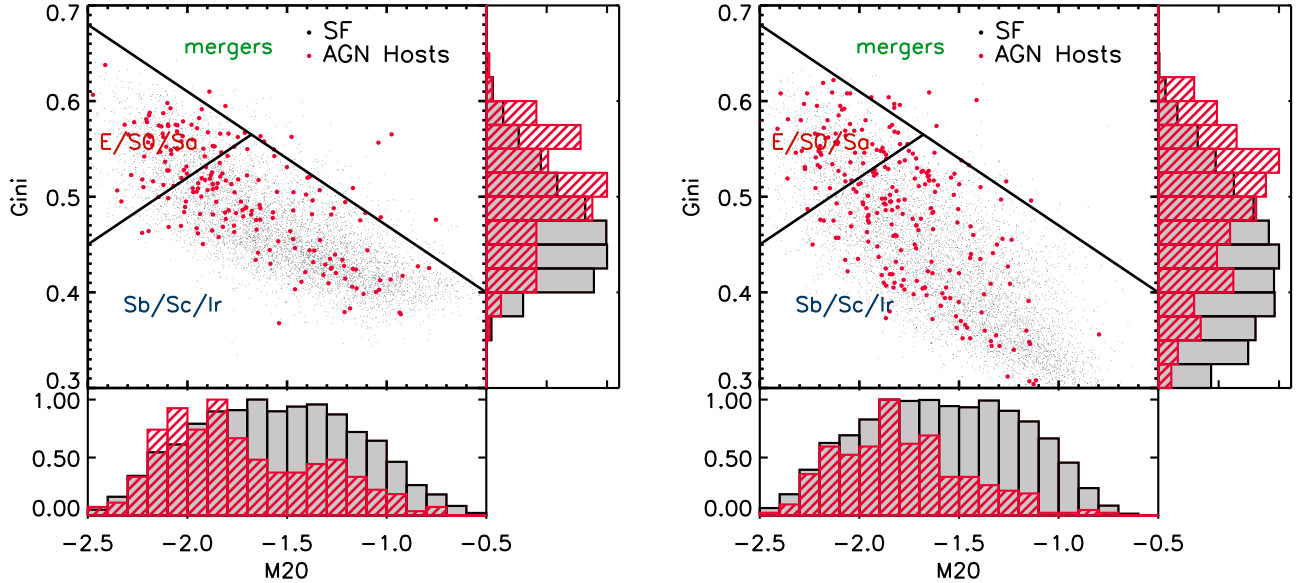


Figure 15. Gini vs. M_{20} plot at $0.5 < z < 1.5$ and $\log M_*/M_\odot > 10.5$. The left plot shows the value from the Zurich Structure & Morphology catalog (Sargent et al. 2007; Scarlata et al. 2007) and the right plot shows the value from Cassata et al. (2007) catalog. The majority of AGN hosts are not merger-like according to the Gini- M_{20} classification.

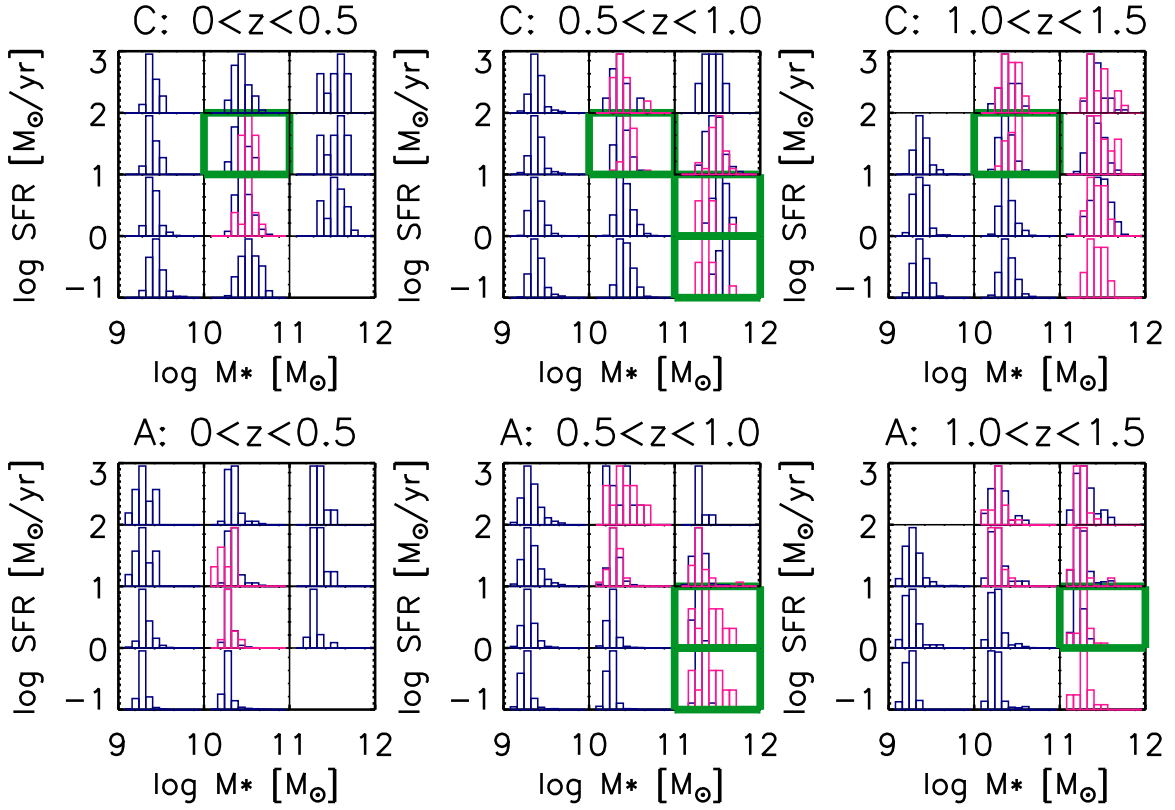


Figure 16. Morphology parameters (concentration and asymmetry) histogram and K–S tests for 12 bins of stellar mass and SFR, and three redshift ranges. The SFR and stellar mass plots are separated into 12 bins according to the borders of the subplot to show the histogram in each bin. The purple histogram represents AGN hosts and the blue histogram represents normal star-forming galaxies. The thick (green) boxes highlight the distributions that are significantly different ($P_{K-S} < 0.05$).

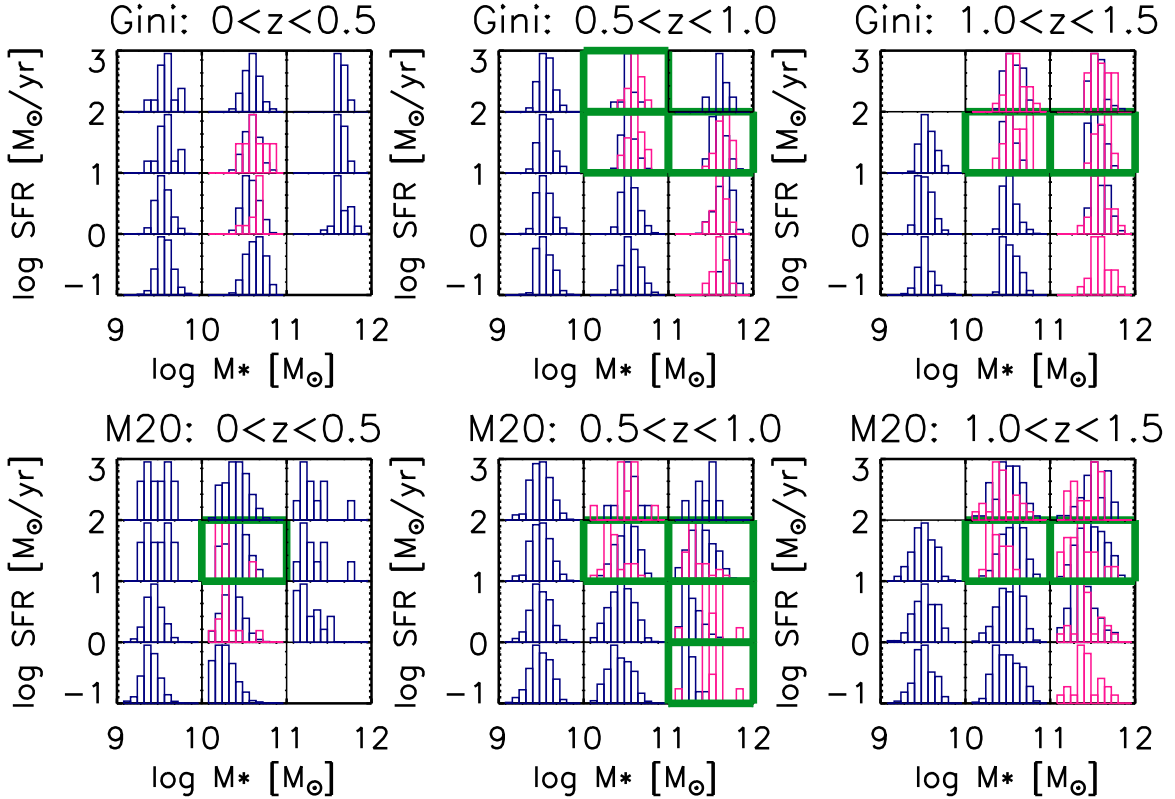


Figure 17. Morphology parameters (Gini and M_{20}) histogram and K–S tests for 12 bins of stellar mass and SFR, and three redshift ranges. The SFR and stellar mass plots are separated into 12 bins according to the borders of the subplot to show the histogram in each bin. The purple histogram represents AGN hosts and blue histogram represents normal star-forming galaxies. The thick (green) boxes highlight the distributions that are significantly different ($P_{K-S} < 0.05$).

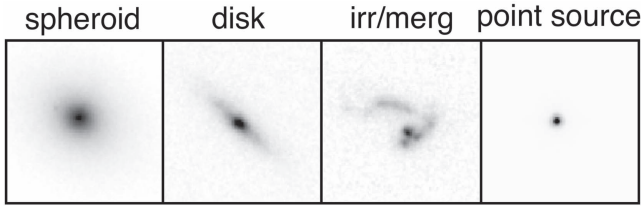


Figure 18. Example of morphology class of *HST*/ACS imaging in our visual classification: disk, spheroid, irregular/merger, and point source. The box size is $6'' \times 6''$.

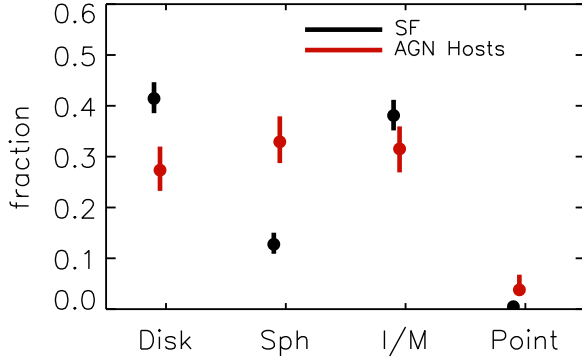


Figure 19. Visual classification for AGNs and star-forming galaxies at $0.5 < z < 1.5$ and $\log M_*/M_\odot > 10.5$. The error bars represent the 68.3% binomial confidence limits as described in Cameron (2011). The merger fraction of AGN hosts is not higher than that of normal star-forming galaxies.

(Grogin et al. 2005; Pierce et al. 2007). More recent studies consider the central nucleus light and show similar (Böhm et al. 2013; Fan et al. 2014; Villforth et al. 2014) or flatter (Schawinski et al. 2011; Simmons et al. 2012) radial light distribution of AGNs compared to inactive galaxies. However, recent results also show that the consideration of AGN contribution can be overestimated, and it is difficult to separate the central bulge and the nucleus light (Rosario et al. 2015; Bruce et al. 2016). Therefore, obscured AGNs provide a robust sample to measure the optical light of host galaxies (Chang et al. 2017). We noted that the majority of our AGN hosts are at $10.5 < \log M_*/M_\odot < 11$, and the most significant difference is also caused by these objects. The different sample selection and stellar mass range might explain the different results by Rosario et al. (2015), which showed that X-ray-selected AGNs have slightly diskier light profiles than inactive galaxies at $z \sim 1$ and a red central light enhancement at $z \sim 2$. The matched stellar masses and redshifts ensure an unbiased selection in our sample. As a sanity check of the selection bias at $24 \mu\text{m}$ between galaxies with and without AGNs, we tested galaxies above a luminosity threshold at $24 \mu\text{m}$ by subtracting the AGN contribution from the SEDs. This ensures that we remove a possible population of passive galaxies hosting AGNs, which are selected at $24 \mu\text{m}$ because of the accretion disk emission. We recalculated the size and Sérsic index dependences with this sample, and still find very similar results to those in Figures 12 and 13, that is, AGN host galaxies are more compact than normal galaxies.

From a morphological point of view, we investigated the two-dimensional surface brightness modeling and nonparametric methods. The obscured AGN host galaxies are smaller, more compact, more asymmetric, and more bulge-like than the control sample. At $z \sim 1$, we found that a 20%–50% AGN

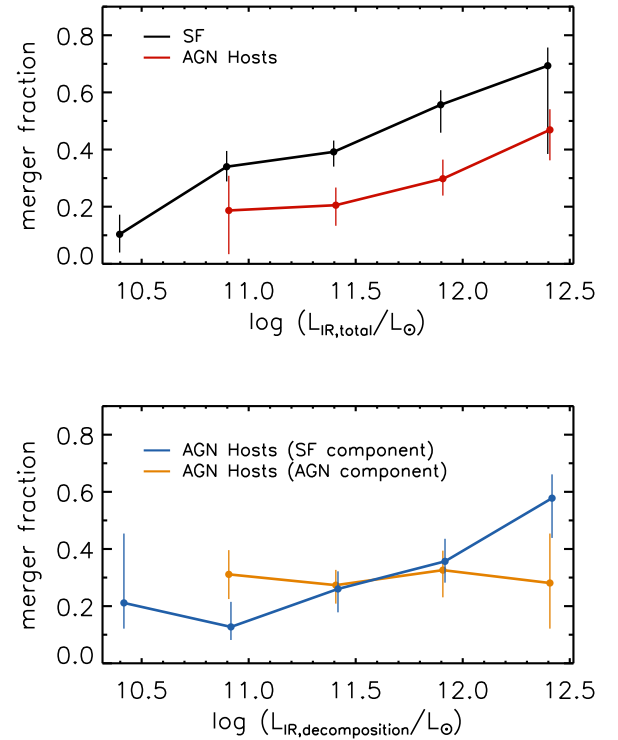


Figure 20. Upper panel: merger fraction from visual classification as a function of total IR luminosity for IR-AGN hosts (red) and star-forming galaxies (black) at $0.5 < z < 1.5$ and $\log M_*/M_\odot > 10.5$. Lower panel: merger fraction in the IR-AGN population as a function of AGN (orange) and star-forming (blue) IR luminosity obtained from our SED decomposition. The error bars in each bin represent the 68.3% binomial confidence limits as described in Cameron (2011). These two plots show that the merger fraction depends on the total and star-forming IR luminosity, rather than on the decomposed AGN IR luminosity.

contribution corresponds to a size decrease of 25%–50%. The correlation between AGN bolometric fraction and structural parameters implies that the AGN activity can be the cause of compactness. Besides, the lack of correlation between obscuration and structural parameters might be a hint that the morphological differences between AGN hosts and the control sample also happens to less obscured AGNs. However, we still have to be careful to consider the AGN contribution of unobscured samples in future works. Moreover, the distribution of structural parameters shows significant differences at several stellar mass, SFR, and redshift bins through K–S tests, and we also found a higher fraction of spheroidal-like host galaxies compared to a control sample of star-forming galaxies by visual classification. This result confirmed our previous finding in Chang et al. (2017), that is, obscured AGN hosts are more compact compared to the control sample.

In the compaction scenario (Tacchella et al. 2016), galaxies live through one or more blue nugget phases in which a minimum in gas depletion time and a maximum in gas fraction are reached. As shown in Figures 8 and 9, the most massive and $z < 1.5$ obscured AGNs are slightly above the main sequence, which is consistent with the scenario of the blue nugget phase. The lower sSFR at $10.5 < \log M_*/M_\odot < 11$ at higher redshifts can be explained by the hypothesis that the sSFR fluctuates down and up several times before it eventually quenches beyond the green valley (Zolotov et al. 2015). Our results suggest that this scenario can also happen to $z \sim 1$ obscured AGN hosts, especially those resulting from IR

selections. Since the fueling of central AGNs might be affected (Dubois et al. 2015), our results on the physical properties, such as the stellar mass-weighted age, extinction, and dust properties, could also provide further constraints on the compaction scenario.



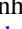







6. Summary

In this paper, we provided a detailed study of IR-selected AGNs. We found that the hosts of these AGNs are not exactly the same as normal star-forming galaxies, both from their physical properties and morphology. We confirm our previous structural results about obscured AGNs. Our main findings are as follows.

1. IR-AGNs and obscured IR-AGNs are located within, or maybe slightly above, the star-forming sequence at $z \sim 1$.
2. Besides the SFR, obscured AGNs show significantly different distributions for several physical parameters from SED fitting, such as stellar mass-weighted age, attenuation, and IR properties. This suggests that obscured AGNs can be in a distinct evolutionary stage from X-ray-selected AGNs.
3. According to the correlation between bolometric AGN fraction and structural parameters, a 20% AGN contribution corresponds to a radius decrease of 24% and a Sérsic index increase of 18%, and a 50% AGN contribution corresponds to a radius decrease of 50% and a Sérsic index increase of 47%.
4. We do not find high merger rates in the whole obscured AGN samples, which includes non-X-ray-detected sources. However, the merger rate of the most luminous AGNs ($\log(L_{\text{IR}}/L_{\odot}) \sim 12.5$) can be up to ~ 0.5 . The increasingly disturbed features with IR luminosity are consistent with previous findings on Compton-thick AGNs. We conclude that the high merger fraction may only apply to the most luminous and heavily obscured AGN hosts, but not to the whole obscured AGN sample.
5. Merger fraction has no dependence on the AGN IR luminosity derived from our SED decomposition. This implies that most obscured AGNs might be triggered by internal mechanisms, such as secular process, disk instabilities, and compaction.
6. We confirm our previous finding about compact obscured AGNs at $z \sim 1$. Our results on the sSFR show that massive obscured AGNs are slightly above the main-sequence population at $z < 2$. This implies that they might be in the blue nuggets phase and affected by fluctuation in the compaction scenario. The differences in the physical properties between obscured AGNs and the control sample may provide further constraints on the compaction scenario.
7. We make publicly available the SED modeling results for all available objects in the COSMOS2015 catalog.

We thank the referee as well as D. Elbaz and A. Dekel for helpful comments and discussions. We acknowledge financial support from Agence Nationale de la Recherche (contract #ANR-12-JS05-0008-01) and the Ministry of Science and Technology of Taiwan grant (105-2112-M-001-029-MY3). We gratefully acknowledge the contributions of the entire COSMOS collaboration. The COSMOS team in France acknowledges support from the Centre National d'Études Spatiales.

ORCID iDs

Yu-Yen Chang  <https://orcid.org/0000-0002-6720-8047>
 Stéphanie Juneau  <https://orcid.org/0000-0002-0000-2394>
 Elisabete da Cunha  <https://orcid.org/0000-0001-9759-4797>
 Mara Salvato  <https://orcid.org/0000-0001-7116-9303>
 Stefano Marchesi  <https://orcid.org/0000-0001-5544-0749>
 Olivier Ilbert  <https://orcid.org/0000-0002-7303-4397>
 Yoshiki Toba  <https://orcid.org/0000-0002-3531-7863>
 Wei-Hao Wang  <https://orcid.org/0000-0003-2588-1265>
 Megan C. Urry  <https://orcid.org/0000-0002-0745-9792>
 Jeyhan S. Kartaltepe  <https://orcid.org/0000-0001-9187-3605>

References

- Abraham, R. G., van den Bergh, S., & Nair, P. 2003, *ApJ*, **588**, 218
 Aird, J., Coil, A. L., Moustakas, J., et al. 2012, *ApJ*, **746**, 90
 Alexander, D. M., & Hickox, R. C. 2012, *NewAR*, **56**, 93
 Azadi, M., Coil, A. L., Aird, J., et al. 2017, *ApJ*, **835**, 27
 Böhm, A., Wisotzki, L., Bell, E. F., et al. 2013, *A&A*, **549**, A46
 Bongiorno, A., Maiolino, R., Brusa, M., et al. 2014, *MNRAS*, **443**, 2077
 Bongiorno, A., Schulze, A., Merloni, A., et al. 2016, *A&A*, **588**, A78
 Breiman, L., Friedman, J., Olshen, R., & Stone, C. 1984, *Classification and Regression Trees* (Monterey, CA: Wadsworth and Brooks)
 Brightman, M., Nandra, K., Salvato, M., et al. 2014, *MNRAS*, **443**, 1999
 Brinchmann, J., Charlot, S., White, S. D. M., et al. 2004, *MNRAS*, **351**, 1151
 Bruce, V. A., Dunlop, J. S., Mortlock, A., et al. 2016, *MNRAS*, **458**, 2391
 Brusa, M., Bongiorno, A., Cresci, G., et al. 2015, *MNRAS*, **446**, 2394
 Brusa, M., Civano, F., Comastri, A., et al. 2010, *ApJ*, **716**, 348
 Calistro Rivera, G., Lusso, E., Hennawi, J. F., & Hogg, D. W. 2016, *ApJ*, **833**, 98
 Cameron, E. 2011, *PASA*, **28**, 128
 Cassata, P., Guzzo, L., Franceschini, A., et al. 2007, *ApJS*, **172**, 270
 Ceverino, D., Dekel, A., & Bournaud, F. 2010, *MNRAS*, **404**, 2151
 Chabrier, G. 2003, *PASP*, **115**, 763
 Chang, Y.-Y., Le Floc'h, E., Juneau, S., et al. 2017, *MNRAS*, **466**, L103
 Chang, Y.-Y., van der Wel, A., da Cunha, E., & Rix, H.-W. 2015, *ApJS*, **219**, 8
 Cisternas, M., Jahnke, K., Inskip, K. J., et al. 2011, *ApJ*, **726**, 57
 Civano, F., Marchesi, S., Comastri, A., et al. 2016, *ApJ*, **819**, 62
 Conselice, C. J. 2003, *ApJS*, **147**, 1
 Coppin, K., Pope, A., Menéndez-Delmestre, K., et al. 2010, *ApJ*, **713**, 503
 da Cunha, E., Charlot, S., & Elbaz, D. 2008, *MNRAS*, **388**, 1595
 da Cunha, E., Walter, F., Smail, I. R., et al. 2015, *ApJ*, **806**, 110
 Daddi, E., Dickinson, M., Morrison, G., et al. 2007, *ApJ*, **670**, 156
 Dale, D. A., Helou, G., Magdis, G. E., et al. 2014, *ApJ*, **784**, 83
 Dekel, A., Birnboim, Y., Engel, G., et al. 2009, *Natur*, **457**, 451
 Del Moro, A., Alexander, D. M., Bauer, F. E., et al. 2016, *MNRAS*, **456**, 2105
 DiPompeo, M. A., Myers, A. D., Hickox, R. C., Geach, J. E., & Hainline, K. N. 2014, *MNRAS*, **442**, 3443
 Donley, J. L., Koekemoer, A. M., Brusa, M., et al. 2012, *ApJ*, **748**, 142
 Dubois, Y., Volonteri, M., Silk, J., et al. 2015, *MNRAS*, **452**, 1502
 Elbaz, D., Daddi, E., Le Borgne, D., et al. 2007, *A&A*, **468**, 33
 Ellison, S. L., Teimoorinia, H., Rosario, D. J., & Mendel, J. T. 2016, *MNRAS*, **458**, L34
 Fan, L., Fang, G., Chen, Y., et al. 2014, *ApJL*, **784**, L9
 Fan, L., Han, Y., Fang, G., et al. 2016, *ApJL*, **822**, L32
 Fiore, F., Puccetti, S., Brusa, M., et al. 2009, *ApJ*, **693**, 447
 Gabor, J. M., Impey, C. D., Jahnke, K., et al. 2009, *ApJ*, **691**, 705
 Georgakakis, A., Nandra, K., Yan, R., et al. 2008, *MNRAS*, **385**, 2049
 Goulding, A. D., Forman, W. R., Hickox, R. C., et al. 2014, *ApJ*, **783**, 40
 Grogin, N. A., Conselice, C. J., Chatzichristou, E., et al. 2005, *ApJL*, **627**, L97
 Harrison, C. M., Alexander, D. M., Mullaney, J. R., et al. 2012, *ApJL*, **760**, L15
 Hernán-Caballero, A., Alonso-Herrero, A., Hatziminaoglou, E., et al. 2015, *ApJ*, **803**, 109
 Hickox, R. C., Jones, C., Forman, W. R., et al. 2009, *ApJ*, **696**, 891
 Hickox, R. C., Mullaney, J. R., Alexander, D. M., et al. 2014, *ApJ*, **782**, 9
 Hickox, R. C., Myers, A. D., Brodwin, M., et al. 2011, *ApJ*, **731**, 117
 Hopkins, P. F., Hernquist, L., Cox, T. J., & Kereš, D. 2008, *ApJS*, **175**, 356
 Huang, T. C., Goto, T., Hashimoto, T., Oi, N., & Matsuhara, H. 2017, *MNRAS*, **471**, 4239
 Ilbert, O., Armouts, S., Le Floc'h, E., et al. 2015, *A&A*, **579**, A2
 Ilbert, O., Capak, P., Salvato, M., et al. 2009, *ApJ*, **690**, 1236

- Ilbert, O., McCracken, H. J., Le Fèvre, O., et al. 2013, [A&A](#), **556**, A55
- Juneau, S., Dickinson, M., Bournaud, F., et al. 2013, [ApJ](#), **764**, 176
- Kartaltepe, J. S., Dickinson, M., Alexander, D. M., et al. 2012, [ApJ](#), **757**, 23
- Kirkpatrick, A., Pope, A., Alexander, D. M., et al. 2012, [ApJ](#), **759**, 139
- Kirkpatrick, A., Pope, A., Charmandaris, V., et al. 2013, [ApJ](#), **763**, 123
- Kirkpatrick, A., Pope, A., Sajina, A., et al. 2015, [ApJ](#), **814**, 9
- Kocevski, D. D., Brightman, M., Nandra, K., et al. 2015, [ApJ](#), **814**, 104
- Kocevski, D. D., Faber, S. M., Mozena, M., et al. 2012, [ApJ](#), **744**, 148
- Lacy, M., Petric, A. O., Sajina, A., et al. 2007, [AJ](#), **133**, 186
- Lacy, M., Storrie-Lombardi, L. J., Sajina, A., et al. 2004, [ApJS](#), **154**, 166
- Laigle, C., McCracken, H. J., Ilbert, O., et al. 2016, [ApJS](#), **224**, 24
- Lanzuisi, G., Perna, M., Delvecchio, I., et al. 2015a, [A&A](#), **578**, A120
- Lanzuisi, G., Ranalli, P., Georgantopoulos, I., et al. 2015b, [A&A](#), **573**, A137
- Le Floc'h, E., Aussel, H., Ilbert, O., et al. 2009, [ApJ](#), **703**, 222
- Lotz, J. M., Davis, M., Faber, S. M., et al. 2008, [ApJ](#), **672**, 177
- Lotz, J. M., Jonsson, P., Cox, T. J., et al. 2011, [ApJ](#), **742**, 103
- Lotz, J. M., Primack, J., & Madau, P. 2004, [AJ](#), **128**, 163
- Lusso, E., Comastri, A., Vignali, C., et al. 2011, [A&A](#), **534**, A110
- Lusso, E., Hennawi, J. F., Comastri, A., et al. 2013, [ApJ](#), **777**, 86
- Mahoro, A., Pović, M., & Nkundabakura, P. 2017, [MNRAS](#), **471**, 3226
- Marchesi, S., Civano, F., Elvis, M., et al. 2016, [ApJ](#), **817**, 34
- Mateos, S., Alonso-Herrero, A., Carrera, F. J., et al. 2012, [MNRAS](#), **426**, 3271
- Mendez, A. J., Coil, A. L., Aird, J., et al. 2013, [ApJ](#), **770**, 40
- Merloni, A., Bongiorno, A., Brusa, M., et al. 2014, [MNRAS](#), **437**, 3550
- Messias, H., Afonso, J., Salvato, M., Mobasher, B., & Hopkins, A. M. 2012, [ApJ](#), **754**, 120
- Messias, H., Afonso, J. M., Salvato, M., Mobasher, B., & Hopkins, A. M. 2014, [A&A](#), **562**, A144
- Mullaney, J. R., Alexander, D. M., Goulding, A. D., & Hickox, R. C. 2011, [MNRAS](#), **414**, 1082
- Mullaney, J. R., Pannella, M., Daddi, E., et al. 2012, [MNRAS](#), **419**, 95
- Noeske, K. G., Weiner, B. J., Faber, S. M., et al. 2007, [ApJL](#), **660**, L43
- Pedregosa, F., Varoquaux, G., Gramfort, A., et al. 2011, *Journal of Machine Learning Research*, **12**, 2825 (arXiv:1201.0490)
- Peng, C. Y., Ho, L. C., Impey, C. D., & Rix, H.-W. 2002, [AJ](#), **124**, 266
- Peng, C. Y., Ho, L. C., Impey, C. D., & Rix, H.-W. 2010, [AJ](#), **139**, 2097
- Perna, M., Brusa, M., Salvato, M., et al. 2015, [A&A](#), **583**, A72
- Peth, M. A., Lotz, J. M., Freeman, P. E., et al. 2016, [MNRAS](#), **458**, 963
- Pierce, C. M., Lotz, J. M., Laird, E. S., et al. 2007, [ApJL](#), **660**, L19
- Polletta, M., Tajer, M., Maraschi, L., et al. 2007, [ApJ](#), **663**, 81
- Prieto, M. A., Reunanen, J., Tristram, K. R. W., et al. 2010, [MNRAS](#), **402**, 724
- Ricci, C., Bauer, F. E., Treister, E., et al. 2017, [MNRAS](#), **468**, 1273
- Ricci, C., Ueda, Y., Koss, M. J., et al. 2015, [ApJ](#), **815**, 13
- Richards, G. T., Lacy, M., Storrie-Lombardi, L. J., et al. 2006, [ApJS](#), **166**, 470
- Rosario, D. J., McIntosh, D. H., van der Wel, A., et al. 2015, [A&A](#), **573**, A85
- Rosario, D. J., Santini, P., Lutz, D., et al. 2013, [ApJ](#), **771**, 63
- Salvato, M., Ilbert, O., Hasinger, G., et al. 2011, [ApJ](#), **742**, 61
- Sanders, D. B., Soifer, B. T., Elias, J. H., et al. 1988, [ApJ](#), **325**, 74
- Santini, P., Rosario, D. J., Shao, L., et al. 2012, [A&A](#), **540**, A109
- Sargent, M. T., Carollo, C. M., Lilly, S. J., et al. 2007, [ApJS](#), **172**, 434
- Scarlata, C., Carollo, C. M., Lilly, S., et al. 2007, [ApJS](#), **172**, 406
- Schawinski, K., Urry, M., Treister, E., et al. 2011, [ApJL](#), **743**, L37
- Schreiber, C., Pannella, M., Elbaz, D., et al. 2015, [A&A](#), **575**, A74
- Scoville, N., Aussel, H., Brusa, M., et al. 2007, [ApJS](#), **172**, 1
- Simmons, B. D., Urry, C. M., Schawinski, K., Cardamone, C., & Glikman, E. 2012, [ApJ](#), **761**, 75
- Stanley, F., Harrison, C. M., Alexander, D. M., et al. 2015, [MNRAS](#), **453**, 591
- Stern, D., Eisenhardt, P., Gorjian, V., et al. 2005, [ApJ](#), **631**, 163
- Suh, H., Civano, F., Hasinger, G., et al. 2017, [ApJ](#), **841**, 102
- Tacchella, S., Dekel, A., Carollo, C. M., et al. 2016, [MNRAS](#), **457**, 2790
- Toba, Y., Nagao, T., Kajisawa, M., et al. 2017, [ApJ](#), **835**, 36
- Treister, E., Schawinski, K., Urry, C. M., & Simmons, B. D. 2012, [ApJL](#), **758**, L39
- Treister, E., Urry, C. M., & Virani, S. 2009, [ApJ](#), **696**, 110
- Ueda, Y., Akiyama, M., Ohta, K., & Miyaji, T. 2003, [ApJ](#), **598**, 886
- Villforth, C., Hamann, F., Rosario, D. J., et al. 2014, [MNRAS](#), **439**, 3342
- Villforth, C., Hamilton, T., Pawlik, M. M., et al. 2017, [MNRAS](#), **466**, 812
- Virani, S. N., De Robertis, M. M., & VanDalsen, M. L. 2000, [AJ](#), **120**, 1739
- Zamojski, M., Yan, L., Dasyra, K., et al. 2011, [ApJ](#), **730**, 125
- Zolotov, A., Dekel, A., Mandelker, N., et al. 2015, [MNRAS](#), **450**, 2327